

Article

The Seven Sisters Hydrothermal System: First Record of Shallow Hybrid Mineralization Hosted in Mafic Volcaniclasts on the Arctic Mid-Ocean Ridge

Ana Filipa A. Marques^{1,2,*}, Desiree L. Roerdink¹, Tamara Baumberger³ ,
Cornel E. J. de Ronde⁴, Robert G. Ditchburn⁴, Alden Denny¹, Ingunn H. Thorseth¹,
Ingeborg Okland¹, Marvin D. Lilley⁵, Martin J. Whitehouse⁶ and Rolf B. Pedersen¹

¹ K.G. Jebsen Centre for Deep Sea Research, University of Bergen, 5007 Bergen, Norway; Desiree.Roerdink@uib.no (D.L.R.); aldenenny42@gmail.com (A.D.); Ingunn.Thorseth@geo.uib.no (I.H.T.); Ingeborg.okland@radgivende-biologer.no (I.O.); rolf.pedersen@geo.uib.no (R.B.P.)

² Vol. Fellow, Commonwealth Scientific and Industrial Research Organization (CSIRO) Mineral Resources, 26 Dick Perry Avenue, Kensington, Perth, WA 6155, Australia

³ NOAA/PMEL & CIMRS, Oregon State University, 2115 SE OSU Drive, Newport, OR 97365, USA; tamara.baumberger@noaa.gov

⁴ GNS Science, 1 Fairway Drive, Avalon, P.O. Box 30-368, Lower Hut 6315, New Zealand; Cornel.deRonde@gns.cri.nz (C.E.J.d.R.); r.ditchburn@gns.cri.nz (R.G.D.)

⁵ School of Oceanography, University of Washington, Seattle, 98195-7940 WA, USA; lilley@u.washington.edu

⁶ Department of Geosciences, Swedish Museum of Natural History, SE-10405 Stockholm, Sweden; martin.whitehouse@nrm.se

* Correspondence: filipa.marques@csiro.au

Received: 28 April 2020; Accepted: 13 May 2020; Published: 15 May 2020



Abstract: We document the discovery of an active, shallow, seafloor hydrothermal system (known as the Seven Sisters Vent Field) hosted in mafic volcaniclasts at a mid-ocean ridge setting. The vent field is located at the southern part of the Arctic mid-ocean ridge where it lies on top of a flat-topped volcano at ~130 m depth. Up to 200 °C phase-separating fluids vent from summit depressions in the volcano, and from pinnacle-like edifices on top of large hydrothermal mounds. The hydrothermal mineralization at Seven Sisters manifests as a replacement of mafic volcaniclasts, as direct intraclast precipitation from the hydrothermal fluid, and as elemental sulfur deposition within orifices. Barite is ubiquitous, and is sequentially replaced by pyrite, which is the first sulfide to form, followed by Zn-Cu-Pb-Ag bearing sulfides, sulfosalts, and silica. The mineralized rocks at Seven Sisters contain highly anomalous concentrations of ‘epithermal suite’ elements such as Tl, As, Sb and Hg, with secondary alteration assemblages including silica and dickite. Vent fluids have a pH of ~5 and are Ba and metal depleted. Relatively high dissolved Si (~7.6 mmol/L Si) combined with low (0.2–0.4) Fe/Mn suggest high-temperature reactions at ~150 bar. A $\delta^{13}\text{C}$ value of -5.4‰ in CO_2 dominated fluids denotes magmatic degassing from a relatively undegassed reservoir. Furthermore, low CH_4 and H_2 (<0.026 mmol/kg and <0.009 mmol/kg, respectively) and $^3\text{He}/^4\text{He}$ of ~8.3 R/Ra_{corr} support a MORB-like, sediment-free fluid signature from an upper mantle source. Sulfide and secondary alteration mineralogy, fluid and gas chemistry, as well as $\delta^{34}\text{S}$ and $^{87}\text{Sr}/^{86}\text{Sr}$ values in barite and pyrite indicate that mineralization at Seven Sisters is sustained by the input of magmatic fluids with minimal seawater contribution. $^{226}\text{Ra}/\text{Ba}$ radiometric dating of the barite suggests that this hydrothermal system has been active for at least 4670 ± 60 yr.

Keywords: seafloor hydrothermal system; volcaniclast-hosted VMS; fluid chemistry; radiometric dating

1. Introduction

Modern seafloor hydrothermal systems are a source of Fe-Cu-Zn-Pb-(Au-Ag) and, like their ancient volcanogenic massive sulfide (VMS) analogues, are formed by the discharge of modified seawater-derived hydrothermal fluids heated by underlying magmas that precipitate metal-rich sulfides on, or near, the seafloor (e.g., [1–3]). Metals leached from source rocks exert control on the fluid and sulfide chemistry in most hydrothermal systems, with Cu + Fe + Co + Ni being predominant in mafic-ultramafic settings and Zn + Pb ± Ag ± As ± Sb ± Hg ± Ba dominating more evolved volcanic settings in arcs and backarcs [4]. However, leaching of the host rock volcanics alone fails to explain metal contents in some giant or high-grade ancient VMS deposits [2]. Thus, it has been suggested that magmatic fluids may be a critical source of ore metals for seafloor hydrothermal systems and their ancient analogues, as even a small amount of metal-rich magmatic fluid introduced in a seafloor hydrothermal system can play an important role in mineralization [2,5,6]. Magmatic degassing of volatiles and metals occur at, or just below, the seafloor during submarine volcanic eruptions [7–12]. More recently, studies have provided evidence for metal transport in the pre-erupted magma and degassing processes beneath seafloor hydrothermal systems [2,13–16]. These magmatic signatures have been especially recognized in arc-related submarine hydrothermal systems, some [17–20] with submarine epithermal style mineralization comparable to subaerial magmatic-hydrothermal systems [4,16,21–26].

Here, we describe the Seven Sisters vent field, which is a shallow (130 mbsl), relatively high-temperature (~200 °C at 130 mbsl) seafloor hydrothermal system hosted by mafic volcanoclasts within a slow spreading mid-ocean ridge on the Kolbeinsey segment of the Arctic Mid-Ocean Ridge (AMOR). At Seven Sisters, we document a spatial and temporal connection between explosive mafic volcanism, magmatic degassing, and creation of magmatic-hydrothermal mineralization with an epithermal-suite signature. These findings may have important implications for ancient VMS deposit classification and exploration guidelines.

2. Geological Setting

The AMOR, which extends from north of the Arctic Circle at 66° N to the Siberian Shelf in the Laptev Sea, is composed of several shorter ridge segments that, from south to north, include the following: the Kolbeinsey Ridge, Mohns Ridge, Knipovich Ridge, and the Gakkel Ridge [27,28] (Figure 1A). The AMOR is spreading at ultraslow rates (<20 mm/yr) with spreading rates decreasing northwards from 18 mm/yr at the Kolbeinsey Ridge to 11 mm/yr at the Gakkel Ridge [29]. The southern part of the ridge system is thought to be strongly influenced by the Iceland hot spot, which results in progressive shallowing of the ridge southward.

Over the last two decades, several hydrothermal sites have been found along the AMOR (e.g., [28,30], and references therein) that are hosted by mafic to serpentinitized ultramafic lithologies, at various depths with varying local sediment influence.

The Kolbeinsey Ridge is a ~540 km long super-segment that extends from the Tjörnes Fracture Zone north of Iceland (~66.5° N) towards the Jan Mayen Fracture Zone at 71° N (Figure 1A). This southernmost part of the Arctic MOR system is characterized by an anomalously thick crust (7–10 km) [31] and a neovolcanic zone that is unusually shallow (<1000 mbsl). The super-segment is itself divided into three segments (i.e., south, central, and north) that are separated by two non-transform offsets at 69° N and 70.7° N, respectively [32].

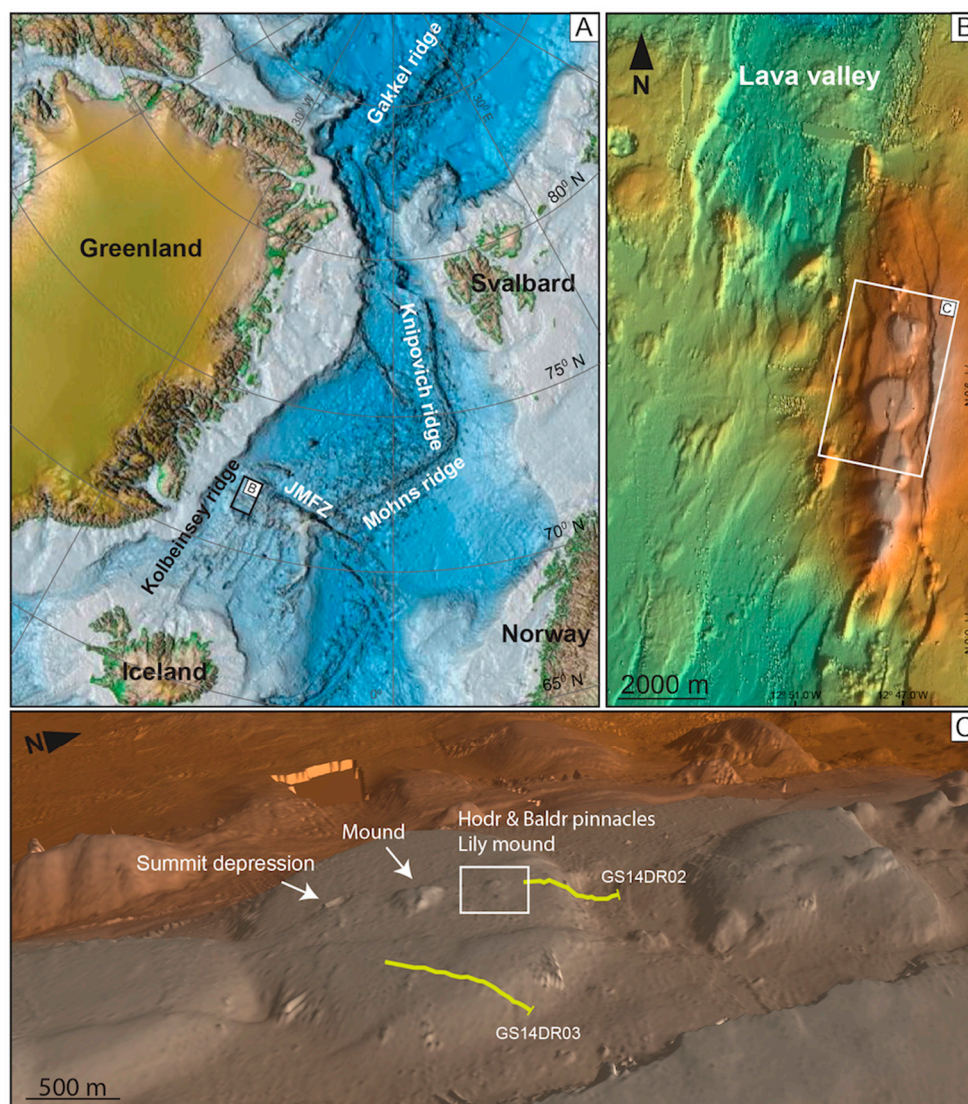


Figure 1. (A) Map of the Arctic Mid-Ocean Ridge (AMOR) system depicting the Knipovich and Mohns Ridges north of the Jan Mayen fracture zone (JMFZ) and Kolbeinsey Ridge south of the JMFZ. The black rectangle at the northern Kolbeinsey Ridge marks the study area that is shown in more detail in (B,C); (D) high-resolution bathymetry of the spreading axis showing a chain of aligned flat-top volcanoes at the eastern margin of the rift depression; (C) high-resolution bathymetry of the flat top volcano that hosts the Seven Sisters hydrothermal system with a summit depression and a central area with venting pinnacles and mounds. Yellow lines mark the dredge paths GS14DR02 and GS14DR03, and white rectangle marks the area where Hodr, Baldr, and Lily mound samples were taken.

The Seven Sisters vent field is located on the Northern Kolbeinsey Ridge within an especially shallow part known as the Eggvin Bank. A recent ocean bottom seismometer (OBS) survey across the Eggvin Bank documented an igneous crustal thickness of up to 13 km [33]. The shallowest part of the Eggvin Bank is less than 30 m deep and is defined by a large volcanic edifice with a summit caldera [34]. Large, recent lava flows fill the rift valley to the north of the summit caldera. The Seven Sisters vent field is located approximately 20 km north of the summit crater at a depth of 130 m along a chain of flat-topped central-type volcanic edifices that follow the eastern margin of the rift valley (Figure 1B,C).

3. Materials and Methods

Seven Sisters hydrothermal system was discovered in 2013 by a team of scientists from the University of Bergen, with the field revisited and further sampled in 2014 [35]. During both cruises, the R/V *G.O. Sars* mapped the hydrothermal field with multibeam sonar, and further explored the area with both an autonomous underwater vehicle (AUV) and a remotely operated vehicle (ROV).

3.1. Mapping

Bathymetric soundings of the Seven Sisters vent field were collected using the EM302 multibeam echo sounder (Kongsberg Maritime AS, Kongsberg, Norway) onboard the R/V *G.O. Sars*. All data were acquired using Kongsberg Seafloor Information Systems (SIS) software and included backscatter reflectivity and water column soundings. The data were then processed in Caris HIPS (Hydrographic Information Processing System) software suite using a standard hydrographic workflow. The water column data were processed and visualized in the Fledermaus FM Midwater package, typically in a 'stacked' view that collapsed all water column soundings to an integrated view at the nadir position of the line. This allowed the relatively disorganized bubble plumes found at Seven Sisters to be readily identified, and then more accurately located to identify the individual vent sites prior to AUV and ROV exploration. To reveal and characterize seabed fluid flow features, we collected sonar data using the HiSAS 1030 (2013) and HiSAS 1032 (2014) interferometric synthetic aperture sonar (SAS) [36] carried by the *FFI Hugin* 1000 AUV. The HiSAS system is a dual-stave interferometric sidescan sonar that operates at a centre frequency of 100 kHz and a bandwidth of 30 kHz. During data acquisition, the *Hugin* was pre-programmed to travel in a survey grid pattern at a speed of approximately 1 m/s, following the terrain and mapping the seafloor systematically from an altitude of 20–30 m above the seafloor. A high-resolution SAS image is formed by combining dynamically focused data from multiple along-track pings. This creates a sonar image of the seafloor with a constant resolution, independent of the sounding distance from the vehicle. The SAS imagery was produced using the FOCUS processing toolbox [37], and the Kongsberg Maritime-developed post processing software *Reflection* was used to combine multiple SAS images into geo-referenced mosaics of large areas of the seafloor.

3.2. Rock and Fluid Sampling

Dredging operations (referenced as 13DR1, GS14DR2, and GS14DR3) each sampled >50 kg of rocks from the western, northern, and eastern flanks of the field, respectively (Figure 1C; Table 1). Thirteen rock samples were collected from the active part of the Seven Sisters vent field using the ROV (Table 1). ROV dive GS14ROV02 surveyed the GS14DR2 dredge area; ROV dives GS14ROV03 and GS14ROV14 to GS14ROV18 surveyed and sampled rocks, fluids, and gases from the smoking craters, as well as mounds and venting pinnacles on the summit of the Seven Sisters flat-top volcano. Sample GS14ROV14R1 was collected from the top of Hodr (Höðr) pinnacle. Samples GS14ROV14R2/R3/R4 were taken from the Baldr (Balðr) pinnacle's top, middle, and base, respectively. Samples GS14ROV15R1 to R4 were taken from a phase-separating venting mound named Lily mound, together with samples GS14ROV15R5 and R6, the latter being more distal to the active venting orifice.

Table 1. Reference, location, and brief description of samples collected from the Seven Sisters hydrothermal system, northern Kolbeinsey Ridge, using a remotely operated vehicle (ROV) and dredges. Sample reference numbers refer to unique specimens of ROV samples and multiple rock specimens of the same type in the dredge collection.

Sample Reference		Latitude	Longitude	Depth (m)	Area	Observations
<i>ROV</i>						
GS14ROV03R1		71° 08.844 N	12° 47.440 W	n.a.	Pinnacle	Mineralized, polymictic, scoriaceous breccia
GS14ROV03R2		71° 08.844 N	12° 47.440 W	n.a.	Pinnacle	Volcaniclastic breccia
GS14ROV03R3		71° 08.844 N	12° 47.440 W	n.a.	Pinnacle	Mineralized, polymictic, scoriaceous breccia
GS14ROV14R1		71° 08.974' N	12° 47.312' W	141	Hodr pinnacle	Barite-pyrite-silica breccia
GS14ROV14R2		71° 08.990' N	12° 47.343' W	132	Baldr pinnacle	Vuggy barite-pyrite
GS14ROV14R3		71° 08.990' N	12° 47.343' W	132	Baldr pinnacle	Vuggy barite-pyrite
GS14ROV14R4		71° 08.991' N	12° 47.354' W	135	Baldr pinnacle	Vuggy silica-barite-pyrite
GS14ROV15R1		71° 08.848' N	12° 47.482' W	130	Lily mound	Vuggy barite-pyrite
GS14ROV15R2		71° 08.848' N	12° 47.482' W	130	Lily mound	Vuggy barite-pyrite
GS14ROV15R3		71° 08.848' N	12° 47.482' W	130	Lily mound	Vuggy barite-pyrite
GS14ROV15R4		71° 08.848' N	12° 47.482' W	130	Lily mound	Vuggy barite-pyrite
GS14ROV15R5		71° 08.839' N	12° 47.466' W	129	Near Lily mound	Mineralized, polymictic, scoriaceous breccia
GS14ROV15R6		71° 08.839' N	12° 47.466' W	129	Near Lily mound	Mineralized, polymictic, scoriaceous breccia
<i>Dredge</i>						
13DR1	Start	71° 08.317' N	12° 48.959' W	284	Western Flank	Mineralized, polymictic, scoriaceous breccia = ROV samples Altered material Altered material Altered material Mineralized, polymictic, scoriaceous breccia/Replacement Mineralized, polymictic, scoriaceous breccia/Crust Mineralized polymictic, scoriaceous breccia = GS14DR03R3
	End	71° 08.926' N	12° 47.321' W	144		
13DR1R1						
13DR1R4						
13DR1R7						
13DR1R8						
13DR1R5						
13DR1R9						
13DR1R10						
GS14DR2	Start	71° 9.2414' N	12° 47.0531' W	215	North Flank	
	End	71° 9.0489' N	12° 47.2782' W	145		
GS14DR2R1						Silica crust
GS14DR2R2						Silica crust
GS14DR2R3						Weathered Fe-oxyhydroxides
GS14DR2R4						Weathered polymictic, scoriaceous breccia (scoria)
GS14DR2R5						Altered polymictic, scoriaceous breccia
GS14DR2R6						Layered, consolidated fresh tuff
GS14DR2R7						Polymictic, scoriaceous breccia
GS14DR3	Start	71° 8.8831' N	12° 46.5321' W	178	East Flank	
	End	71° 8.7272 N	12° 47.1275 W	123		
GS14DR3R1						Weathered Fe-oxyhydroxides
GS14DR3R2						Weathered polymictic, scoriaceous breccia (scoria)
GS14DR3R3						Mineralized, polymictic, scoriaceous breccia
GS14DR3R4						Vesicular basalt

3.3. Geochemical and Mineralogical Analyses

All rock samples were carefully washed with fresh water. Fresh volcanic whole-rock samples were cut using a rock saw and the least altered portions were selected for geochemical analysis. Mineralized rocks were dried in an oven (max. temp. 48 °C) and stored in sealed bags with nitrogen to prevent further oxidation. Fifty-four polished thin sections were prepared and studied under transmitted and reflected light petrographic microscopes. Representative polished sections were carbon-coated and imaged using the University of Bergen's scanning electron microscope (SEM) Zeiss

55 VP Field Emission, complemented by Thermo Noran Liquid N₂ Free detectors allowing for X-ray microanalysis by means of solid-state energy dispersive spectrometry (EDS) (University of Bergen, Norway). Extensive, semi-quantitative SEM-EDS in situ analyses were made of fresh glass shards, sulfides, sulfates, and amorphous silica using Thermo Noran System VI to identify mineral phases too small (<10 µm) for unequivocal detection using simple petrographic microscopes.

Whole-rock geochemistry analyses were undertaken by Actlabs Ltd., Canada (www.actlabs.com) using sodium peroxide fusion followed by induced coupled plasma optical emission spectrometry (ICP-OES); *aqua regia* digestion followed by ICP-OES, ICP-mass spectrometry (MS), and INAA; and cold vapor FIMS. The procedure followed for rock pulverization was as follows: (1) selected samples were cut by diamond saw into small slices <1.5 cm thick, (2) samples were carefully washed and dried at 25 °C, (3) dried samples were crushed using a hammer while enclosed within thick paper envelopes to prevent metal contamination, and (4) small fragments were then powdered in an agate ring mill. Selected samples were manually pulverized using an agate mill and pressed into tablets for analysis using a Bruker D8 X-ray diffractometer at the Department of Chemistry, University of Bergen. Raw spectra and mineral identification were processed in-house using International Centre for Diffraction data (ICDD) mineral database software and later using a different phase identification software, Match! {MatchPhaseIdentify}, giving similar results, which are presented as Supplementary Material (File S1).

3.4. Isotope Geochemistry

Twelve Sr isotope analyses (including two duplicates) of barite-dominated bulk-rock samples were done at the Department of Earth Sciences, University of Bergen. All samples were heated to 1000 °C for one hour in a Carbolite chamber furnace to remove organic impurities. Samples weighing 100 mg each were digested in concentrated HF on a heating plate at 135 °C for 48 h. The HF supernatant was evaporated to dryness and the residues were then hydrolyzed in a weak solution of HNO₃ on a heating plate under sub-boiling-point conditions. This nitrate salt residue was then also evaporated to dryness and completely dissolved in 1 mL 3N HNO₃. Strontium was separated by specific extraction chromatography using Sr-spec resin and analyzed using a Finnigan MAT 262 thermal ionization mass spectrometer. Strontium isotopic ratios were corrected for mass fractionation using a ⁸⁸Sr/⁸⁶Sr value of 8.375209. Repeated measurements of strontium carbonate standard SRM 987 during the analysis yielded an average ⁸⁷Sr/⁸⁶Sr value of 0.710235 ± 9 (2σ; n = 10).

Residual barite (BaSO₄) from the digestions used for Sr isotope analysis was separated from the solutions by centrifugation in 2 mL micro-centrifuge tubes and sent to ACTLABS for δ³⁴S analysis. In addition, in situ sulfur isotope analyses (³²S, ³³S and ³⁴S) were done on 15 pyrite grains from sample 13DR1R1 using a CAMECA IMS-1280 at the Swedish Museum of Natural History (Nordsim facility), Stockholm, Sweden. Sulfur isotopic analyses were performed on polished rock chips mounted in 25 mm diameter epoxy blocks with a 30 nm gold coating. A section was cut from the sample block to allow co-mounting with epoxy-embedded pyrite standards. Measurements followed the analytical protocol of [38] with a 10 kV and ~2 nA Cs⁺ focused primary beam yielding an average spot size of 10 µm. Gold coating was removed during a 90 s pre-sputter over a 20 × 20 µm rastered area, and detector backgrounds were measured for 30 s. Charge build-up on the sample was prevented using a low-energy electron gun. Instrumental mass fractionation was determined by bracketing analyses of unknowns with measurements of Ruttan pyrite, using a δ³⁴S value of 1.408‰ ± 0.006‰ [39]. Sulfur isotopic compositions were calculated as δ³⁴S = [((³⁴S/³²S)_{sample}/(³⁴S/³²S)_{V-CDT}) - 1] × 1000. Analytical precision and data quality are the same as those reported for samples in [40], which were run during the same analytical session.

3.5. Geochronology

Radium isotopes ²²⁶Ra and ²²⁸Ra (with half-lives of 1600 and 5.75 yr) are formed by radioactive decay of ²³⁸U (via ²³⁰Th) and ²³²Th, respectively. Because Ra and Ba are chemically similar, they co-precipitate as barite when hot hydrothermal fluid discharges into and/or mixes with ambient

seawater. From the onset of mineralization, ^{226}Ra and ^{228}Ra decay because they are no longer supported by their radiogenic parent isotopes, ^{230}Th and ^{232}Th , as these are not extracted from rock by hydrothermal interaction [41]. Barite is resistant to seafloor (chemical) weathering so that the decaying ^{226}Ra and ^{228}Ra are undisturbed from the time of barite precipitation, making ^{226}Ra dating of hydrothermal barite an important tool in the investigation of temporal evolution of seafloor hydrothermal systems [16,20,42,43]. In this study, ages for barite mineralization in nine representative samples were determined using the short-lived isotope systems $^{228}\text{Th}/^{228}\text{Ra}$ and $^{228}\text{Ra}/^{226}\text{Ra}$ following the method of [42]. The activity ratios of $^{228}\text{Th}/^{228}\text{Ra}$, $^{228}\text{Ra}/^{226}\text{Ra}$ ($\text{Bq}\cdot\text{Bq}^{-1}$) and $^{226}\text{Ra}/\text{Ba}$ ($\text{Bq}\cdot\text{g}^{-1}$) are used for dating barite in the age ranges 0.3–12, 3–35 and 500–15,000 yr, respectively. The initial $^{226}\text{Ra}/\text{Ba}$ value at any one site, that is, the value at the onset of mineralization, must first be established as it is essential for calculating the age of older mineralization using the decrease in $^{226}\text{Ra}/\text{Ba}$ owing to radioactive decay. Recent studies have shown that the barite present in hydrothermal deposits can have a complex history and that they may form during two or more hydrothermal events with different initial $^{226}\text{Ra}/\text{Ba}$ values. In particular, dissolution and precipitation (remobilization) of barite within the deposit is problematic as barite that gain some or all of their Ba and Ra through such a process may obtain significantly lower initial $^{226}\text{Ra}/\text{Ba}$ values owing to decay of ^{226}Ra in the “old barite” that is being remobilized [44]. Ideally, if there are sufficient samples that still contain ^{228}Ra , an age for the remobilized older barite can be estimated by plotting a $^{226}\text{Ra}/\text{Ba}$ versus $^{228}\text{Ra}/\text{Ba}$ mixing line for two end members that are different in age [44].

3.6. Fluid Chemistry and Dissolved Gases

Measurements of pH, alkalinity, and various compounds (H_2S , NH_4 , NO_3 , NO_2 and PO_4) were made shipboard immediately after fluid sampling. The pH was measured using a portable pH-meter (Metrohm 826) (Metrohm, Herisau, Switzerland), alkalinity was determined by titration using an autotitrator (Metrohm Titrando 888), and the compounds were analyzed by spectrophotometric methods using a QuAatro continuous flow analyzer (SEAL Analytical). Filtered ($\leq 0.2\ \mu\text{m}$) samples were split into aliquots for later analyses of major (Na, K, Mg and Ca), minor (Si, Mn, Fe and Sr), and trace elements (Ni, Co, Cu, Cd, Zn and Pb) that were filled in acid-cleaned HDPE bottles, acidified to 3 vol% HNO_3 and stored at 4 °C until analysed by induced coupled plasma optical emission spectrometry (ICP-OES) (Thermo Finnigan Iris) (Thermo Fisher Scientific, Waltham, MA, USA) and high resolution ICP mass spectrometry (HR-ICP-MS) (Thermo Finnigan Element 2). Aliquots for anions (Cl , SO_4 and Br) were stored at 4 °C in HDPE bottles until analysed by ion chromatography (Metrohm).

Dissolved gases and free gas bubbles were collected using titanium alloy gas-tight bottles connected to a snorkel, or funnel inlet, operated by the ROV. After each dive, the gas-tight samples were processed on a high vacuum line to extract the gas phase and subsample for gas analysis later onshore [45]. Compositional analysis of the gas samples was conducted using gas chromatography at the University of Washington, Seattle. Standard errors for CO_2 , CH_4 , H_2 , N_2 , O_2 , Ne and Ar were $\pm 3\%$ – 5% of the measured value. Extrapolation of the data through zero Mg removes the effects of seawater contamination and provides estimates of the end-member fluid composition [46].

The isotopic compositions of carbon species were determined using a gas chromatograph interfaced with a Thermo ConFlo IV to a Thermo Delta V Plus isotope ratio mass spectrometer at the Geological Institute, ETH Zürich, Switzerland. Isotope values for CH_4 and CO_2 are reported with respect to the standard Vienna Pee Dee Belemnite (VPDB) in the familiar δ notation. Standard deviations are 0.1‰ for $\delta^{13}\text{C}_{\text{CH}_4}$ and 0.2‰ for $\delta^{13}\text{C}_{\text{CO}_2}$. Helium isotopes were determined using a 21 cm radius, dual-collector, sector-type instrument specially designed for helium isotope analysis. The measurements were standardized using a Pacific marine air standard. The $^3\text{He}/^4\text{He}$ ratios are given in R/Ra corr ($\text{R} = ^3\text{He}/^4\text{He}$ and $\text{Ra} = \text{R}^{\text{air}} = 1.4 \times 10^{-6}$), which is the value corrected for atmospheric helium contamination. Precision for $^3\text{He}/^4\text{He}$ values averaged about 0.05 R/Ra . All methods used to determine the gas composition are described in more detail in [47].

4. Results

4.1. Vent Field Architecture

Diffuse venting is widespread on top of the flat top volcano that hosts the Seven Sisters hydrothermal system, although there are three geomorphologically distinct areas that host noticeable hydrothermal activity (Figure 1C): (1) a summit depression (Figure 2A,B); (2) a ~100 m wide central mound with noticeable hydrothermal venting; and (3) clusters of rounded ~20 m wide mound structures (Figure 2C,D), smoking craters and pinnacle-like structures like Hodr and Baldr pinnacles venting clear fluids up to 181 °C (Figure 2E,F). The summit depression is a collapsed structure exposing fractured crusts of volcanoclasts. Gas bubbles and diffuse venting with associated bacterial mat seeps preferentially follow(?) N–S fractures in layered, coarse-grained consolidated volcanoclasts (e.g., Figure 2B). Ochre and white substrates indicate pervasive hydrothermal alteration, weathering, and leaching. Small mound structures, approximately 5 m in diameter and oriented NE along an alignment that begins at the summit depression, vent phase-separating clear fluids at 199 °C and 130 m deep (e.g., Lily mound, Video S1). Some of the larger mounds are partially collapsed, possibly owing to anhydrite dissolution. Outside the hydrothermal mound areas, dark volcanoclastic material fills fractures suggest recent explosive volcanic activity. The northern flank of the flat top volcano reveals a gravitational collapse (not shown) that exposes altered units with unconformable crusts of layered volcanoclasts on top.

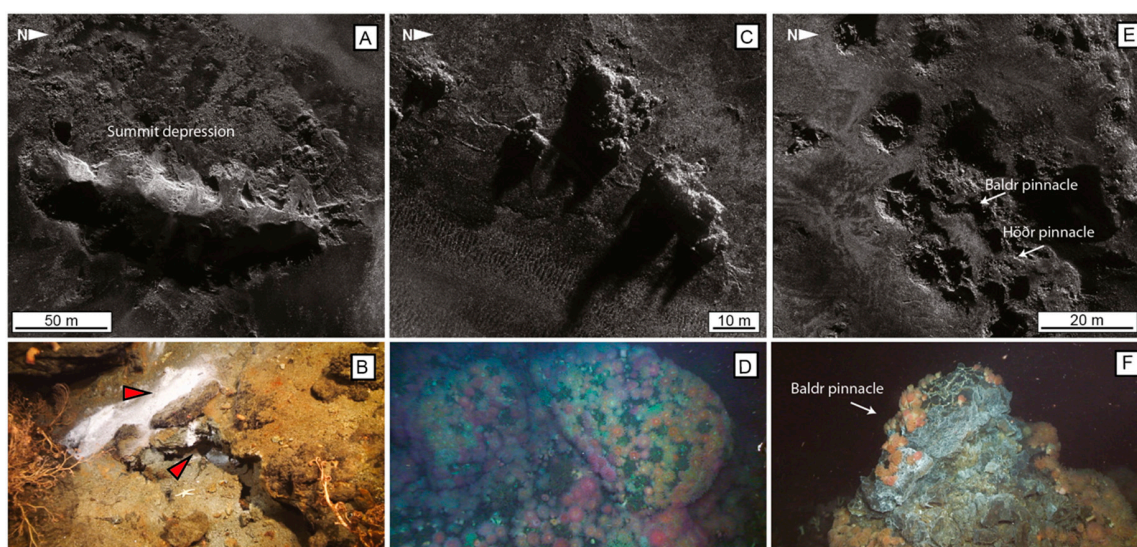


Figure 2. Hi-synthetic aperture sonar (SAS) acoustic imaging (A,C,E) and corresponding remotely operated vehicle (ROV) high definition video still frames (B,D,F) of the Seven Sisters hydrothermal system, as in Figure 1 (C); (A,B) summit depression where ROV observations confirmed diffuse venting through fractured, coarse-grained volcanoclastic material that was covered by white bacterial mats (red arrows); (C,D) rounded hydrothermal structures covered by anemones; (E,F) pinnacle-like hydrothermal structures venting ~181 °C clear fluids.

4.2. Petrography

The samples collected along the flat-topped volcanic edifice include vesicular basalt, consolidated volcanoclasts (Figure 3A), vuggy barite-pyrite-silica and mineralized polymictic, scoriaceous breccia (Figure 3B–H), silica crusts (Figure 3I), and hydrothermally altered material (Figure 3J). We also find a correlation between rocks collected by dredging and those sampled by ROV (see Table 1).

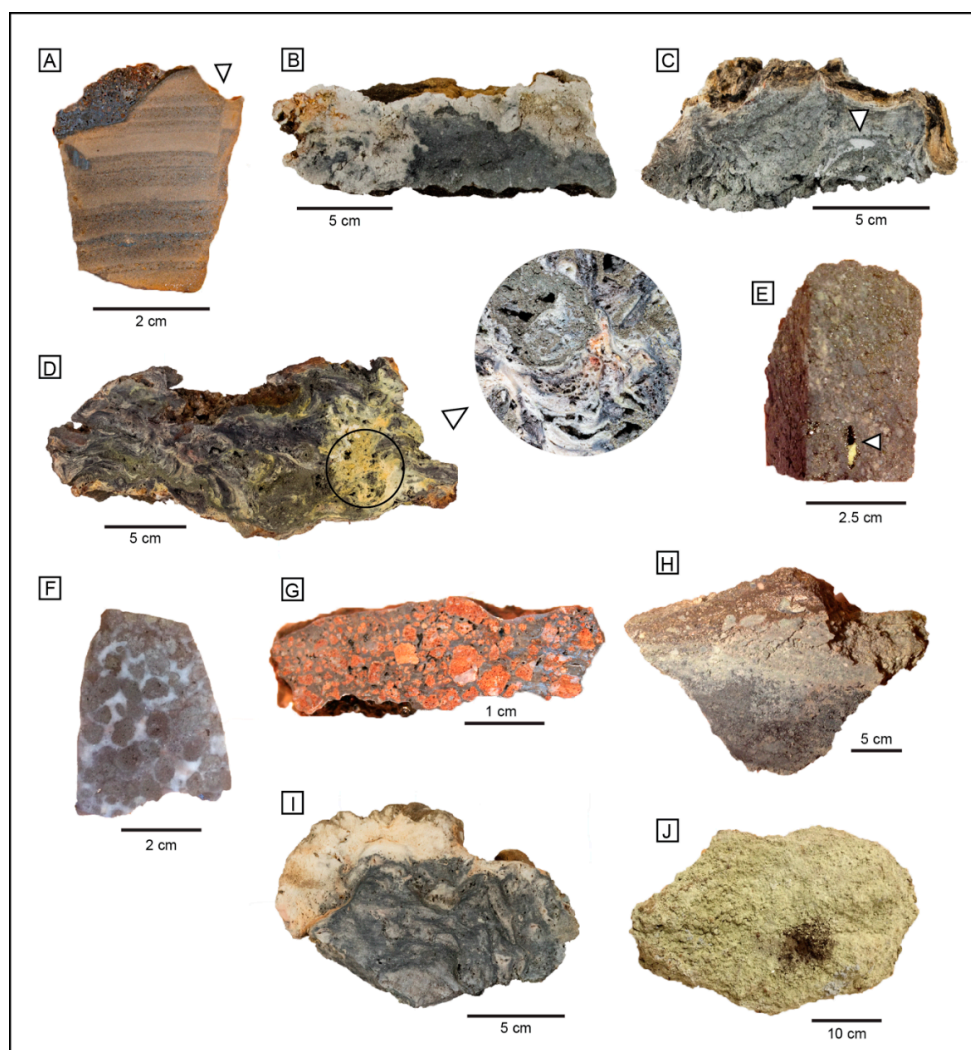


Figure 3. Representative lithotypes sampled at Seven Sisters. (A) Relatively fresh, laminated, clast-supported shard-rich tuff (GS14DR2R6; arrow points to sealed micro-fault); (B) barite-pyrite-silica breccia (GS14ROV14R1) sampled from the actively venting Hodr pinnacle showing zonation owing to the predominance of barite (white) on the exterior and sulfide and silica (grey) in the interior of the sample; (C) vuggy barite-pyrite-silica sample (GS14ROV15R2) from the Lily mound venting phase-separating fluids (arrow points to an area infilled with silica filaments and spherules); (D) vuggy barite-pyrite-silica (GS14ROV14R4) sampled from the base of Baldr pinnacle, this sample shows a pyrite-rich domain (GS14ROV14R4y) and a darker, more silica-rich domain (GS14ROV14R4b), and the arrow points to a close-up where vuggy silica is interlaid with sulfide; (E) mineralized volcaniclastic breccia (GS13DR1R1) with native sulfur in cavity (white arrow); (F) scoriaceous mineralized breccia cemented by anhydrite (GS13DR1R10); (G) oxidized scoriaceous breccia example of (F) now cemented by Mn-oxide phases; (H) mineralized volcaniclastic breccia (GS13DR1R5), showing sulfide mineralization replacement from the bottom towards the top, and mantled by a layer of polymictic, heterogranular, and volcaniclastic material; (I) silica crust (GS14DR2R2), showing color zonation mostly owing to the presence of impurities; and (J) friable, pale-yellow volcanic-sedimentary altered material with textural similarities to volcaniclastic breccias.

4.2.1. Basaltoid Scoria

A vitrophyric, highly vesicular fresh basalt scoria fragment was sampled on the eastern flank of the volcano. Plagioclase phenocrysts are dominant, ranging from a few glomerocrysts up to 1.5 mm in width, to euhedral micro-laths measuring less than 100 μm . Subhedral to euhedral plagioclase, and subhedral olivine and clinopyroxene phenocrysts ($\sim 500 \mu\text{m}$ width) with corroded rims, suggest

melt-crystal disequilibrium. The groundmass is glassy and host vesicles with a bimodal size distribution with approximate diameters of 500 μm and 100 μm , suggestive of a two-stage vesiculation event.

4.2.2. Consolidated Volcaniclasts with Vitriclastic Textures

A relatively fresh, laminated (<1 cm thick), clast-supported, shard-rich tuff was sampled on the northern flank of the volcano (Figure 3A). The well-sorted layers are of uneven thickness and alternate between darker, finer shards and lighter, coarser-grain shards. The shards are mostly cusate (Figure 4A), but also platy and scoria-shaped, some with contorted vesicles, and may host minor phenocrysts (i.e., ~5% plagioclase; <1% olivine and pyroxene) or primary magmatic sulfide droplets. The glass is isotropic and yellow in thin section, typical of sideromelane. Mn-crust covers the consolidated volcaniclasts and contains two unidentified Mn-oxide phases forming fine, botryoidal, concentric aggregates (Figure 4B). These glass shards are similar to those found in the mineralized breccias described below.

4.2.3. Mineralized Samples

Mineralized polymictic scoriaceous breccia, vuggy barite-pyrite, and vuggy silica-pyrite materials make up both pinnacles and mounds (Figure 3B–H) and are ubiquitous in dredged samples. These rocks are matrix-supported and polymictic, depicting varying degrees of hydrothermal alteration and seafloor weathering (e.g., Figure 3F,G).

The mineralization sequence is similar in all the studied mineralized lithotypes. That is, varying degrees of sulfide-sulfate mineralization are seen, ranging from less than 5% to almost complete replacement of the volcaniclastic rock. Figure 3H shows a mineralized rock in which a sulfide mineralization “front” (bottom grey) moves upwards, replacing altered volcaniclastic material (pale green). The top of the sample is composed of weathered material exposed to the seafloor.

The volcaniclastic components are mostly scoriaceous clasts, commonly ~1 mm (Figure 4D), but up to 1 cm wide (Figure 3F–G), and commonly contain contorted vesicles (Figure 4C,D), including variable proportions of euhedral to subhedral phenocrysts (i.e., plagioclase > clinopyroxene > olivine) and microphenocrysts. Also present are rounded lithic clasts with trachytic texture. Different clast types depict varying degrees of alteration (e.g., Figure 4C); some appear unaltered, although many show signs of palagonitization suggesting multiple volcanic events and post-depositional reworking of the unconsolidated deposit prior to hydrothermal mineralization. Semi-quantitative *in situ* SEM-EDS analysis on fresh glass shards shows approximate basanite compositions with 41 wt.% SiO_2 , 13 wt.% Al_2O_3 , 5.5 wt.% MgO , 6.5 wt.% FeO , 1.3 wt.% TiO_2 , 7.3 wt.% CaO , 0.9 wt.% K_2O , and 2.9 wt.% Na_2O , corroborating the mafic nature of the volcaniclastics.

Barite and minor anhydrite are the major hydrothermal mineral phases present in the samples. Anhydrite crystals are euhedral, presenting as large prisms (Figure 4C,D), whereas barite crystals are euhedral, but show different growth habits from early, large, tabular crystals (Figure 4E), to sheath-like to late-stage radial fibrous arrangements (Figure 4F).

Pyrite is ubiquitous, preferentially found in the vesicles of the glass shards (Figure 4G,H) and rimming grain boundaries (Figure 5A), and is the first sulfide to form (Figure 5B). Pyrite can be euhedral, pseudomorph lamellar after barite, and framboidal. Small (10 μm), cubic pyrite crystals grow inside the volcaniclastic vesicles until the original vesicular texture is entirely replaced by massive pyrite up to 2 mm in size (Figure 4G,H). Larger pyrite grains are zoned, subhedral, and intergrown with marcasite. A second stage of sulfide mineralization is characterized by the occurrence of sphalerite, chalcopyrite, galena, and Ag-sulfosalts (Figure 5C–I). These phases are typically smaller, between 10 and 20 μm , and mantle pyrite rims (Figure 5C,D) precipitate after barite (Figure 5E,G) or are characterized by fine, dendrite-like disseminations within spherules of micro and cryptocrystalline silica (Figure 5H,J). Fe-poor, translucent sphalerite grains, commonly associated with chalcopyrite, are anhedral when rimming pyrite and barite. However, if sphalerite has grown into open spaces, it tends to be spherical in habit, exhibiting botryoidal growth (Figure 5H).

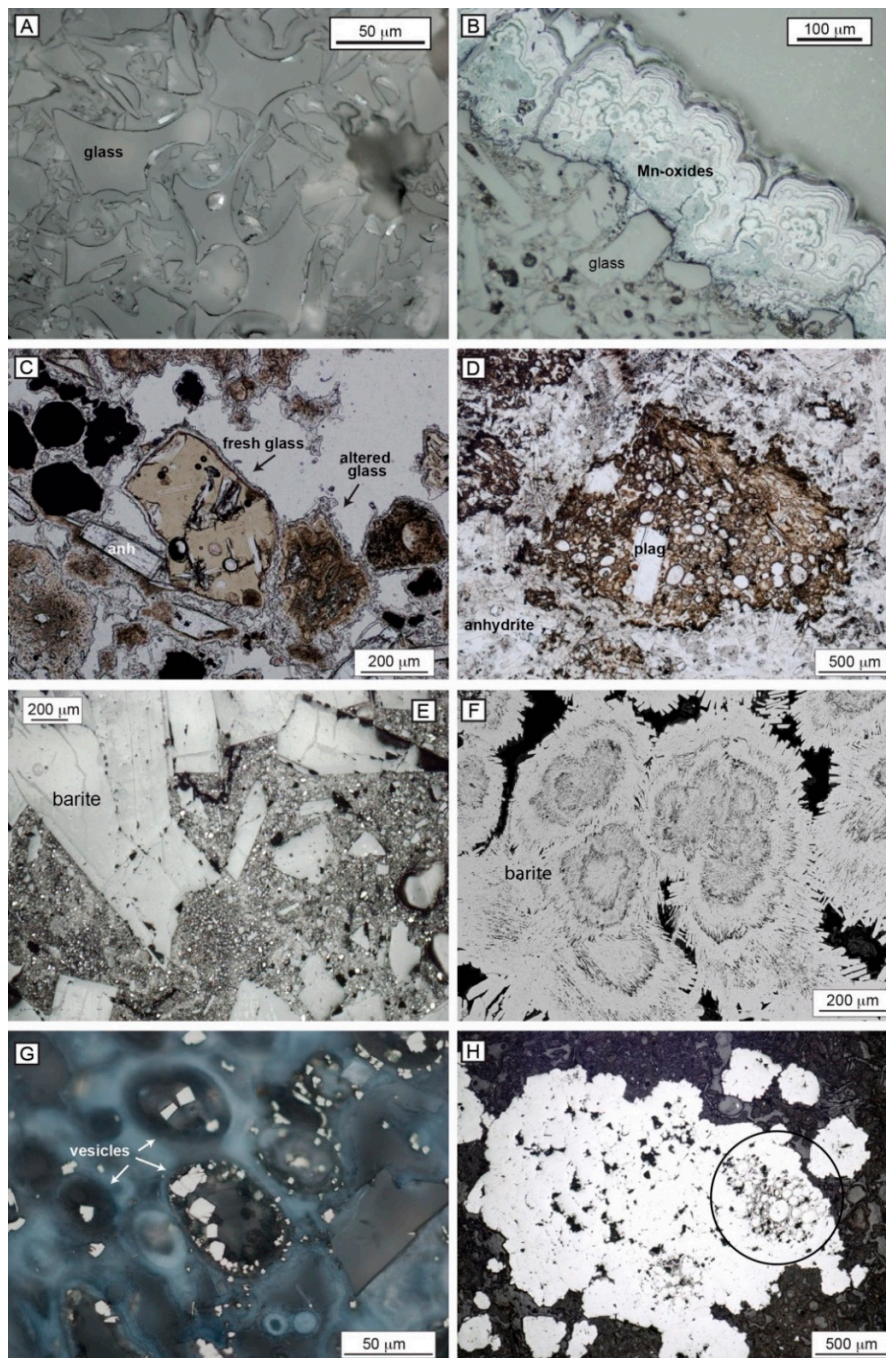


Figure 4. Photomicrographs of tuff and mineralized samples under transmitted (TL) and reflected light (RL). (A) Detail of cusped shards on the laminated clast-supported shard-rich tuff (GS14DR2R6) (RL); (B) botryoidal Mn-oxides rimming glassy shards in a tuff (GS14DR2R6) (RL); (C) fresh, glassy volcaniclastic with few vesicles and plagioclase phenocrysts next to altered, vesicular, glassy volcaniclastic, and tabular anhydrite and sulfides (opaque) (13DR1R9) (TL); (D) example of a highly vesicular, altered volcaniclastic with plagioclase phenocrysts and contorted vesicles on the top, cemented by anhydrite (13DR1R10) (TL); (E) large barite laths cemented by much smaller, fragmented barite indicative of mechanical weathering (GS14R14R3) (RL); (F) scanning electron microscope (SEM) backscatter electron mode (BSE) image of detail of radiating tabular crystals of barite indicative of quench structures where seawater has mixed with hydrothermal fluid (GS14R14R2) (RL); (G) detail of the volcaniclastic vesicles being progressively infilled by euhedral pyrite crystals (13DR1R10) (RL); and (H) massive pyrite aggregates still exhibiting relic volcaniclastic textures (circle, center right) (13DR1R5) (RL). plag = plagioclase; anh = anhydrite.

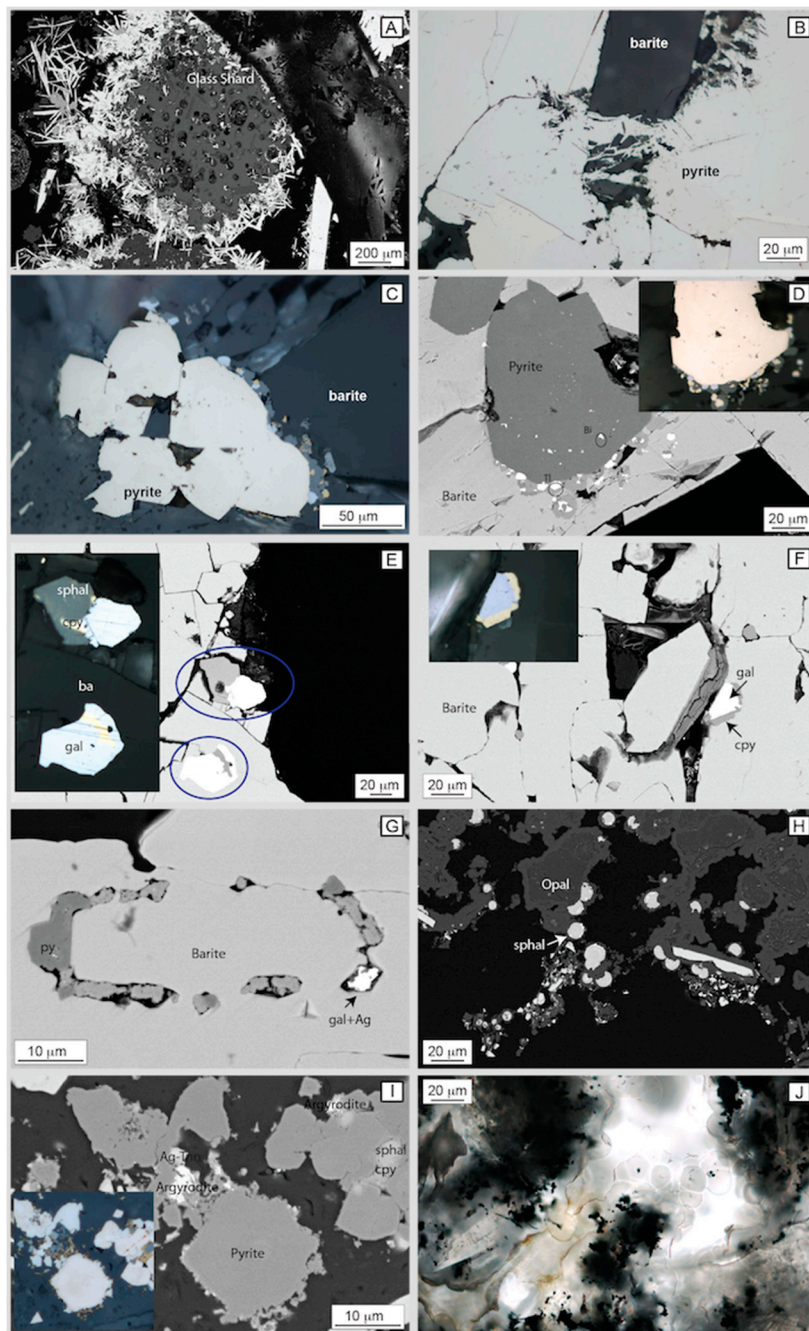


Figure 5. Photomicrographs of mineralized samples under transmitted and reflected light and SEM. (A) Backscatter electron mode (BSE) of (darker) glass shards being replaced by tabular crystals of (whiter, or more reflectant) barite; (B) detail of fracturing and replacement of barite by pyrite; (C) subhedral pyrite grains rimmed by chalcopyrite (yellow), sphalerite (dark grey), and galena (light grey) surrounded by barite; (D) combined BSE and reflected light (insert) photomicrographs of pyrite in barite crystal rimmed by sphalerite, chalcopyrite, and galena with Tl and Bi peaks identified in the energy dispersive spectrometry (EDS) spectra; (E) combined BSE and reflected light (insert) photomicrographs of galena-chalcopyrite and galena-chalcopyrite-sphalerite composite grains within barite; (F) combined BSE and reflected light (insert) photomicrographs of galena rimmed by chalcopyrite within barite; (G) pyrite and Ag-rich galena growing between the grain boundaries of barite; (H) late-stage, open-space botryoidal sphalerite (white reflectant material) and cryptocrystalline silica (dark material); (I) combined BSE and reflected light (insert) photomicrographs of pyrite crystals rimmed by late-stage chalcopyrite, sphalerite, argentotennantite, and argyrodite; and (J) microcrystalline silica in transmitted light coating fine-grain sulfides. Sphal = sphalerite, gal = galena, cpy = chalcopyrite, Ag-tnn = argentotennantite, and agy = argyrodite.

Subhedral galena appears as epitactic growths on pyrite grains (Figure 5C,D) or intergrown with chalcopyrite (Figure 5F) and is associated with Au and Ag peaks on EDS spectra. Other Au peaks detected in the EDS spectra were associated with amorphous silica, barite, and chalcopyrite. Sulfosalts have been identified through SEM-EDS semi-quantitative analysis as argento-tennantite and argyrodite (Figure 5I). In addition, there are other very small (less than 1 μm wide) unidentified sulfide phases bearing Pb-Ag, As-Pb, Bi-S, Tl, Mo and Au.

4.2.4. Silica Crusts

A dredge on the northern flank of the flat topped volcano recovered a composite sample that included a sacharoid-vuggy, silica-rich layer lying between coarse-grained layers of volcanoclastic material and an Mn-like crust. Smaller in size, but ubiquitous in dredge GS14DR02, were white and grey deposits of silica (Figure 3I, sample GS14DR2R1 and GS14DR2R2). This may correspond to some of the crusts seen around the active vent areas from which warm and diffuse fluids were seen to be discharging. These sinter-like samples are mostly composed of sacharoid, colorless silica interlaid with sub-metallic grey silica (Figure 3I). Silica micro-textures are characterized by both straight and curved 10 μm wide filamentous silica networks of radiating rods, and small (up to 10 μm) spherules of amorphous and cryptocrystalline silica (Figure 5J).

4.2.5. Hydrothermally Altered Material

Dredge 13DR01 sampled many granular, earthy and friable, pale yellow (Figure 3J) to ochre clay-rich samples. These textural features are similar to some of the coarser grain breccias (e.g., Figure 3F), suggesting that some mineralized breccias underwent intense leaching that obliterated most of the primary volcanic-sedimentary textures.

4.3. Geochemistry of Mineralized and Hydrothermally Altered Samples

Whole-rock compositions of representative mineralized samples (Table 2) show that most are low in sulfide sulfur and base metals (i.e., Cu, Zn and Pb) and that silica and Ba are major components with contents of up to 60.5 wt.% and 43.8 wt.%, respectively. Other, typically common major elements such as CaO, MgO, Na₂O, and K₂O are only minor in these samples.

Iron correlates positively with S and is most abundant in the sulfide-rich samples (up to 35.1 wt.% FeO; 33 wt.% S) owing to the pyrite-dominated mineralogy. Pyrite-rich samples are Ba-depleted, but show higher As, Hg, Mo, Tl and Sb contents. Layered sample GS14ROV14R4, subdivided in -b for the silica-rich layer and -y for the pyrite-rich layer, contains the highest As (403 and 1240 ppm) and Sb (334 and 610 ppm) contents, and relatively high Hg (30.9 and 43.3 ppm), Mo (19 and 22 ppm), and Tl (81.5 and 153 ppm). Sample 13DR1R1 shows native sulfur lining a vesicle (Figure 3e) and contains the highest Hg (203 ppm), Mo (36 ppm), and Tl (171 ppm) of all the samples.

Samples collected from the top of the venting structures, that is, Hodr pinnacle (GS14ROV14R1) and Lily mound top (GS14ROV15R1), contain less than 5 wt.% sulfide sulfur and are mostly made up of barite (up to 43 wt.% Ba). They are, however, relatively enriched in Ag and Au (30–125 ppm Ag; 205–278 ppb Au) compared with the remaining samples and have the lowest As-Hg-Mo-Tl-Sb contents. Base metals contents are higher near the top of the vents, but are still low overall (185 ppm Cu, 1690 ppm Zn, and 504 ppm Pb, GS14ROV15R1).

With the exception of high SiO₂ contents (70.6 wt.%), silica crust material is depleted in other major oxide elements. Barium is the second most abundant element (6.29 wt.%) and yet still represents <10% of most silica crusts. Barite grows as euhedral radial blades (rosettes) dispersed within the silica, or as laths aligned in layers. Notwithstanding its low sulfide S content (0.12 wt.% S), the Si-crust sample contains 15 ppm Ag and base-metal contents similar to those found in samples with visible sulfides. The dominant grey layers seen in dredge sample GS14DR2R2 (e.g., Figure 3i) show the presence of minute sulfides coating the silica rods, visible under the petrographic microscope.

The hydrothermally altered material is characterized again by high SiO₂ (61.18 wt.%) and Al₂O₃ (14.28 wt.%) contents, but also with noticeable amounts of Na₂O (1.74 wt.%) and TiO₂ (1.12 wt.%). Traces of Ba are present (800 ppm) and contents of Ga (10 ppm) and Cs (6.85 ppm) are elevated.

Table 2. Whole rock geochemistry of representative rocks from the Seven Sisters hydrothermal system, Arctic Mid-Ocean Ridge.

Reference	GS14D R2R2	GS14ROV 14R1	GS14ROV 14R4b	GS14ROV 14R4y	13D R1R1	GS14ROV 15R1	13D R1R7
Mineralogy Type	Silica ± Barite Si-crust	Sulfide-Sulfate	Sulfide-Sulfate	Sulfide-Sulfate Barite-Pyrite-Silica	Sulfide-Sulfate	Sulfide-Sulfate	Clay Altered
Site Obs.	Dredged	Hodr pinnacle Top	Baldr pinnacle Base	Baldr pinnacle Base	- Dredged	Lily mound Top	Dredged
wt.%							
SiO ₂	70.60	31.23	60.54	17.97	29.74	16.13	61.18
CaO	0.14	0.15	0.20	0.14	0.42	0.20	1.61
FeO	0.27	0.39	14.54	35.12	26.12	2.43	4.93
MgO	0.01	0.08	0.04	<0.01	0.15	0.1	0.88
Na ₂ O	0.08	0.23	0.19	0.12	0.27	0.22	1.74
K ₂ O	0.01	0.04	0.04	0.01	0.06	0.05	0.86
Al ₂ O ₃	0.06	0.68	0.09	0.02	1.91	0.51	14.28
Cr ₂ O ₃	<0.01	<0.01	< 0.01	<0.01	<0.01	<0.01	<0.01
TiO ₂	<0.02	0.05	< 0.01	<0.01	0.20	0.02	1.12
P ₂ O ₅	<0.01	<0.01	< 0.01	<0.01	<0.01	<0.01	0.06
Sum	71.17	32.85	75.64	53.38	58.86	19.65	86.66
Ba	6.29	37.20	7.51	10.30	10.70	43.80	0.08
Fe	0.21	0.3	11.3	27.3	20.3	1.89	3.83
S*	0.12	0.34	12.29	>20.00	>20.00	2.20	0.10
S	1.69	4.18	13.1	33	25.2	4.64	0.12
<i>ppm</i>							
Mn	7	105	28	40	78	40	17
Ni	<1	<1	2	6	5	4	4
Cu	11	77	4	6	21	185	53
Se	<0.1	0.5	0.6	0.9	1.2	0.6	0.4
Zn	62	99	11	16	216	1690	25
Pb	55	85	3	6	5	504	<2
As	19	20	403	1240	116	51	5
Ag	14.8	30.1	1.9	5.6	0.6	125	<0.2
Hg	0.358	12.4	30.9	43.3	203	4.9	0.1
Cd	<0.5	1.2	< 0.5	<0.5	<0.5	6.9	<0.5
Ga	<1	<1	<1	<1	2	4	10
Ge	<0.1	<0.1	<0.1	0.2	0.2	<0.1	1.3
Mo	4	5	19	22	36	3	<2
Sb	11.3	4.8	334	610	74	13.5	4.1
Bi	<0.10	<0.10	<0.10	<0.10	<0.10	<0.10	0.14
Te	<0.1	<0.1	<0.1	<0.1	< 0.1	<0.1	<0.1
Tl	2.1	3.6	81.5	153	171	22.1	0.3
Cs	<0.05	0.07	<0.05	<0.05	0.21	0.2	6.85
<i>ppb</i>							
Au	< 5	205	26	105	37	278	<5

* sulfide sulfur.

X-ray diffraction analysis on bulk powder (File S1) confirmed the mineralogical observations and, furthermore, identified clay minerals (kaolin-group minerals, namely dickite and nacrite) and Si-phases (possibly cristobalite and other SiO₂ phases) not easily classified using standard petrographic techniques. Barite, including a Pb-rich barite variety (also confirmed using SEM-EDS), is ubiquitous in the analyses, followed by pyrite and marcasite as the main sulfide phases. Anhydrite was identified in sample 13DR1R5 (Figure 3H), consistent with petrographic observations.

4.4. Isotope Geochemistry

The results of whole-rock strontium isotope ratios (⁸⁷Sr/⁸⁶Sr) of barite-rich samples and bulk sulfur isotope analyses of barite separates from mineralized samples and silica crusts are given in Table 3. Values for ⁸⁷Sr/⁸⁶Sr show a small range between samples (Figure 6a), from 0.703961 ± 8 to 0.704834 ± 8 (average 0.704308) and lie between modern seawater values and Northern Kolbeinsey Ridge basalt at ~71° N (⁸⁷Sr/⁸⁶Sr = 0.703047; [48]). Sulfide-rich mineralized breccias, which contain native sulfur in

cavities, are the most radiogenic samples ($^{87}\text{Sr}/^{86}\text{Sr} = 0.704834$), whereas the least radiogenic material is the silica crust with $^{87}\text{Sr}/^{86}\text{Sr} = 0.703961$. Lily mound samples have $^{87}\text{Sr}/^{86}\text{Sr}$ values of ~ 0.704140 , Hodr pinnacle top has a $^{87}\text{Sr}/^{86}\text{Sr}$ value of 0.704404, and Baldr pinnacle top and bottom has $^{87}\text{Sr}/^{86}\text{Sr}$ values of 0.704060 and 0.704201, respectively.

Table 3. Strontium and sulfur isotope data for whole rock and barite separates, respectively, from the Seven Sisters hydrothermal system.

	Sample	$^{87}\text{Sr}/^{86}\text{Sr}$	2 σ Error	$^{87}\text{Sr}/^{86}\text{Sr}$ Corrected	$\delta^{34}\text{S}_{\text{SO}_4}$
Mineralized, polymictic, scoriaceous breccia					
Dredged	13DR1R1	0.704824	0.000008	0.704834	
Dredged	13DR1R1	0.704667	0.000009	0.704677	
Dredged	13DR1R1	0.704827	0.000009	0.704831	
<i>Barite-pyrite-silica</i>					
Hodr pinnacle	GS14ROV14R1	0.7044	0.000008	0.704404	24.0
Baldr pinnacle	GS14ROV14R2	0.704054	0.000008	0.704058	21.8
Baldr pinnacle	GS14ROV14R2 *	0.70406	0.000008	0.704062	
Baldr pinnacle (base)	GS14ROV14R4b	0.704192	0.000008	0.704194	
Baldr pinnacle (base)	GS14ROV14R4y	0.704206	0.000009	0.704208	17.8
Lily mound (top)	GS14ROV15R1	0.704087	0.000009	0.704092	22.2
Lily mound (top)	GS14ROV15R2	0.704187	0.000008	0.704189	20.1
Lily mound (top)	GS14ROV15R2 *	0.704184	0.000008	0.704186	
Silica crust					
Dredged	GS14DR2R2	0.703956	0.000009	0.703961	18.1

* duplicate.

Barite $\delta^{34}\text{S}$ values range between 17.8‰ and 24.0‰, ranging to both more negative and positive values relative to modern seawater sulfate (21.5‰) [49]. Lower than seawater $\delta^{34}\text{S}$ values are found at the base of Baldr pinnacle, in silica crust, and the Lily mound. Higher $\delta^{34}\text{S}$ values are from sulfate-bearing samples collected from the top of the Lily mound and from the Hodr and Baldr pinnacle vent conduits.

In situ sulfur isotope analyses of pyrite from one of the mineralized dredge samples (sample 13DR1R1; Table 4) show pyrite $\delta^{34}\text{S}$ values spanning 3.7‰, ranging from -1.6‰ to 2.1‰ , with an average of $0.34\text{‰} \pm 0.64\text{‰}$ ($n = 15$).

4.5. Geochronology

In total, nine samples were used for radiometric dating, which include a Si crust, the top of Hodr pinnacle (2 samples), Baldr pinnacle (3 samples), and Lily mound (3 samples; see Table 5). Recent mineralization ages of <12 yr old are given by the activity ratio $^{228}\text{Th}/^{228}\text{Ra}$, that is, the amount of ^{228}Th grown from deposited ^{228}Ra . Lily mound samples range from 3.6 ± 0.03 to 4.4 ± 0.05 yr, whereas samples from the top of the Hodr and Baldr pinnacles have 6.5 ± 0.8 and 4.1 ± 0.6 yr, respectively. The oldest $^{228}\text{Th}/^{228}\text{Ra}$ mineralization age is given by a sample taken for a section close to the Baldr pinnacle top at 8.1 ± 2.6 yr.

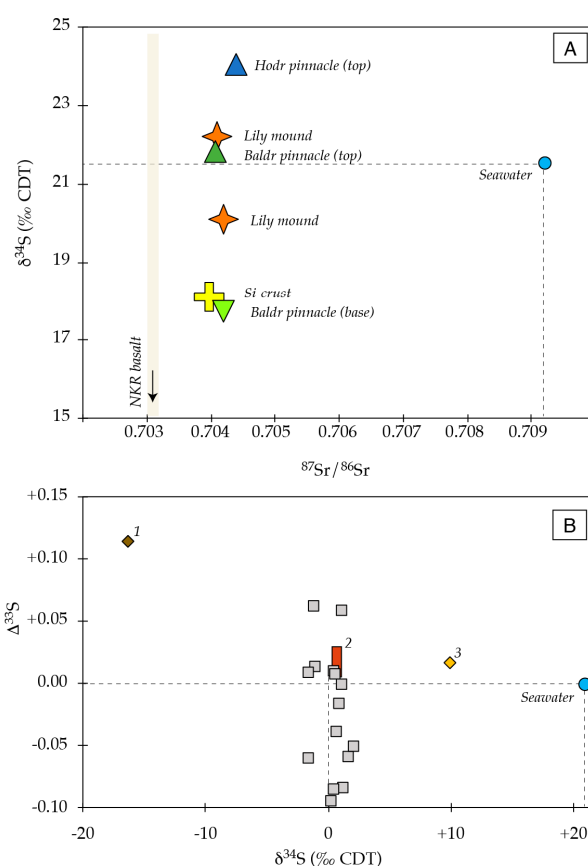


Figure 6. Strontium and sulfur isotope values in sulfate and sulfides from the Seven Sisters hydrothermal system. (A) $^{87}\text{Sr}/^{86}\text{Sr}$ versus $\delta^{34}\text{S}$ in barite; the average $^{87}\text{Sr}/^{86}\text{Sr}$ value for Seven Sisters samples plots within typical hydrothermal barite values (e.g., [43,50]) and show little influence of seawater [51], but are close to the $^{87}\text{Sr}/^{86}\text{Sr}$ value for local basalts [48] from the Northern Kolbeinsey Ridge (NKR); $\delta^{34}\text{S}$ in barite has a greater range, plotting above (top of venting structures) and below seawater values ($\delta^{34}\text{S}$ 21.5; [49]); (B) in situ $\delta^{34}\text{S}$ vs. $\Delta^{33}\text{S}$ in pyrite shows MORB-like $\delta^{34}\text{S}$ close to 0.0‰ (0.34‰ ± 0.64‰) and predominantly negative $\Delta^{33}\text{S}$ values that plot distant from known biogenic pyrite (1; [52]) or hydrothermal pyrite fields (2 and 3; [52,53]).

Table 4. In situ $\delta^{34}\text{S}$ in pyrite from a mineralized breccia, Seven Sisters hydrothermal system.

13DR1R1	Phase	$\delta^{34}\text{S}$	1^{sd}	$\delta^{33}\text{S}$	1^{sd}	$\Delta^{33}\text{S}$	1^{sd}
mt_M02@1	Pyrite	0.72	0.06	0.33	0.06	−0.04	0.07
mt_M02@2	Pyrite	−1.55	0.07	−0.86	0.06	−0.06	0.07
mt_M02@3	Pyrite	−1.03	0.06	−0.52	0.06	0.01	0.07
mt_M02@4	Pyrite	0.50	0.07	0.27	0.06	0.01	0.08
mt_M02@5	Pyrite	−1.61	0.06	−0.82	0.05	0.01	0.07
mt_M02@6	Pyrite	1.67	0.06	0.80	0.06	−0.06	0.07
mt_M02@7	Pyrite	−1.13	0.06	−0.52	0.06	0.06	0.07
mt_M02@8	Pyrite	2.12	0.07	1.04	0.06	−0.05	0.08
mt_M02@9	Pyrite	0.28	0.06	0.05	0.05	−0.09	0.07
mt_M02@10	Pyrite	0.91	0.06	0.45	0.05	−0.02	0.07
mt_M02@11	Pyrite	1.09	0.06	0.62	0.05	0.06	0.07
mt_M02@12	Pyrite	1.12	0.06	0.58	0.05	0.00	0.07
mt_M02@13	Pyrite	0.58	0.06	0.31	0.05	0.01	0.07
mt_M02@14	Pyrite	1.21	0.06	0.54	0.05	−0.08	0.07
mt_M02@15	Pyrite	0.51	0.06	0.18	0.06	−0.08	0.07

Table 5. Ba content, initial ^{226}Ra and ^{228}Ra activities, $^{228}\text{Ra}/^{226}\text{Ra}$ values, and estimated radiometric ages for mineralized samples from Seven Sisters.

Sample Ref.	Area	Composition	Sampled	Ba	$^{228}\text{Ra}/^{226}\text{Ra}$	$^{228}\text{Th}/^{228}\text{Ra}$	$^{226}\text{Ra}/\text{Ba}$	Initial Values		Fraction of Initial $^{226}\text{Ra}/\text{Ba}$ Value	Age (Years)		Recent barite using $^{228}\text{Th}/^{228}\text{Ra}$
								$^{228}\text{Ra}/\text{Ba}$	$^{226}\text{Ra}/\text{Ba}$		minimum age*	mixing line**	
GS14DR2R2	Silica crust	Silica + Barite	23.07.2014	14.5	n.d.	n.d.	6.0 ± 0.2			0.123 ± 0.004	4840 ± 70		
GS14ROV14R1	Hodr pinnacle	Barite + Sulfide + Silica (white)	07.08.2014	40.4	0.023 ± 0.001	1.19 ± 0.06	49.0 ± 0.5	2.49 ± 0.14	49.14 ± 0.51	<- Initial value			6.5 ± 0.8
GS14ROV14R1	Hodr pinnacle	Barite + Sulfide + Silica (grey)	07.08.2014	27.9	n.d.	n.d.	35.3 ± 0.4			0.718 ± 0.011	760 ± 40	3220 ± 560	
GS14ROV14R2	Baldr pinnacle (top)	Barite + Sulfide + Silica	07.08.2014	53.2	0.028 ± 0.003	0.94 ± 0.08	42.8 ± 0.5	1.99 ± 0.20	42.89 ± 0.52	0.871 ± 0.014	320 ± 40	3220 ± 560	4.1 ± 0.6
GS14ROV14R3	Baldr pinnacle	Barite + Sulfide + Silica	07.08.2014	50.4	0.018 ± 0.002	1.29 ± 0.12	38.1 ± 0.4	1.79 ± 0.19	38.28 ± 0.42	0.776 ± 0.012	580 ± 30	3220 ± 560	8.1 ± 2.6
GS14ROV14R4	Baldr pinnacle (base)	Barite + Sulfide + Silica (grey)	07.08.2014	20.6	n.d.	n.d.	6.5 ± 0.1			0.132 ± 0.003	4670 ± 60		
GS14ROV15R1	Lily mound	Barite + Sulfide + Silica	07.08.2014	45.2	0.603 ± 0.007	0.98 ± 0.006	42.2 ± 0.5	43.04 ± 1.81	42.30 ± 0.55	0.859 ± 0.014	350 ± 40	1080 ± 270	4.4 ± 0.05
GS14ROV15R2	Lily mound	Barite + Sulfide + Silica	07.08.2014	51.4	0.772 ± 0.007	0.87 ± 0.004	45.1 ± 0.6	53.77 ± 2.24	45.18 ± 0.56	0.918 ± 0.015	200 ± 40	1080 ± 270	3.6 ± 0.03
GS14ROV15R5	Near Lily mound	Barite + Sulfide + Silica	07.08.2014	36	n.d.	n.d.	29.2 ± 0.3			0.595 ± 0.009	1200 ± 40		

Quoted uncertainties (counting statistics only) are one standard deviation. Ratios and ages are adjusted to sample collection date. Recent mineralization was dated using the $^{228}\text{Th}/^{228}\text{Ra}$ values (^{228}Ra - ^{228}Th disequilibrium). Ages derived from $^{226}\text{Ra}/\text{Ba}$ values are under-estimated because barite is mixture of old and recent mineralization. * Minimum age derived by comparing $^{226}\text{Ra}/\text{Ba}$ values for barite that is a mixture of old and recent mineralization. ** Age of older barite derived from initial $^{228}\text{Ra}/\text{Ba}$ and $^{226}\text{Ra}/\text{Ba}$ values (mixing line for barite of different age).

The lowest $^{226}\text{Ra}/\text{Ba}$ values were measured in the Si-crust ($6 \text{ Bq}\cdot\text{g}^{-1}$), Baldr pinnacle base ($6.5 \text{ Bq}\cdot\text{g}^{-1}$), and a sample close to Lily mound (29 g^{-1}). No ^{228}Ra was detected in these samples. Samples from the top of the actively venting pinnacles and mound have higher $^{226}\text{Ra}/\text{Ba}$ values ($35\text{--}49 \text{ Bq}\cdot\text{g}^{-1}$) with the highest value ($49.0 \pm 0.5 \text{ Bq}\cdot\text{g}^{-1}$) measured from the white section of Hodr's pinnacle top (Figure 3B), corresponding to material least affected by remobilized older barite, and thus decay-corrected to the time of mineralization. This corrected initial $^{226}\text{Ra}/\text{Ba}$ value ($49.14 \pm 0.51 \text{ Bq}\cdot\text{g}^{-1}$) is taken as the initial value when applying the dating method of decreasing $^{226}\text{Ra}/\text{Ba}$ values with time. Dividing the $^{226}\text{Ra}/\text{Ba}$ value of a sample by this initial ratio gives the decay factor used to calculate the age of the older components. However, the ages derived using $^{226}\text{Ra}/\text{Ba}$ values appeared to be much older when compared with those using $^{228}\text{Th}/^{228}\text{Ra}$ values (e.g., $350 \pm 40 \text{ yr}$ vs. $4.4 \pm 0.05 \text{ yr}$ at Lily mound; GS14ROV15R1). However, by combining the Ba, ^{228}Ra , and ^{226}Ra data, we find that these older ages are almost certainly incorrect owing to an inherited component of much older, remobilized barite, and thus an age for the older barite component can be estimated [44].

4.6. Fluid and Gas Chemistry

Hydrothermal fluids venting from Hodr pinnacle and the Lily mound have measured pH values of ~ 5.0 and little alkalinity (i.e., 0.25 mmol/L Hodr pinnacle; 0.04 mmol/L Lily mound) when compared with seawater values (2.4 mmol/L) (Table 6). Fluids collected at both locations contain little Mg ($1.6\text{--}7.9 \text{ mmol/L}$) and SO_4 ($0.13\text{--}0.21 \text{ mmol/L}$), indicating limited mixing with ambient seawater. End-member compositions of clear fluids venting from the Hodr pinnacle at $181 \text{ }^\circ\text{C}$ show relatively higher H_2S ($303.21 \text{ }\mu\text{M}$) and lower chlorinity (529 mmol/L Cl^-) when compared with the phase separating fluids sampled at Lily mound of $200 \text{ }^\circ\text{C}$ ($\sim 120 \text{ M H}_2\text{S}$; 586 mmol/L Cl^-) whose Cl concentrations are greater than those of seawater (540 mmol/L Cl^-). Hodr pinnacle and mound fluids have relatively similar compositions for many elements, although a few components such as H_2S , Ba, and Zn diverge significantly. Unfiltered and filtered samples from the Hodr pinnacle also show different compositions owing to post-sampling precipitation of Cr, Cu and Zn. Hodr fluids contain approximately $3 \text{ }\mu\text{mol/L}$ more base metals (Fe + Cu + Zn + Pb) compared with mound fluids. However, this difference is not so noticeable in dissolved Si, which hardly varies between locations, ranging between 7.34 and 7.89 mmol/L . These values are within the range of several higher temperature and deeper MOR systems [54–56]. Seven Sisters hydrothermal fluids show relatively low Na/Cl values ($0.69\text{--}0.73$) and significantly higher Ca/Cl (0.08) and K/Cl ($0.06\text{--}0.07$) values when compared with seawater (Na/Cl 0.86 ; Ca/Cl 0.02 ; K/Cl 0.02). Strontium mirrors Ca and Sr/Cl values in the fluids (0.0003) and are $\sim 2\text{x}$ higher than seawater (0.00016). Low Fe/Mn values in the Hodr pinnacle and mound samples, at $\sim 1:2$ to $1:5$, respectively, are significantly below values found in most seafloor hydrothermal systems, where Fe/Mn values typically range from $1:1$ to $5:1$ c.f. [57,58].

End member CO_2 concentrations are 2.94 mmol/kg for the Lily mound (ROV18-GT16) and 5.58 mmol/kg for the Hodr pinnacle (ROV15-GT16). End member CH_4 and H_2 concentrations were low in both vents and ranged from 15 to $26 \text{ }\mu\text{mol/kg}$ and 4 to $9 \text{ }\mu\text{mol/kg}$, respectively. Total measured gas concentrations were 3 mmol/kg in the phase-separated vent and 5.1 mmol/kg (corrected for air) in the Hodr pinnacle. A bubble sample collected near Lily mound (ROV16-GT17), an area where bubbles were seen seeping from the seafloor, was dominated by 80.3 \% CO_2 , and further contained $4\% \text{ CH}_4$ and $0.01\% \text{ H}_2$. Carbon isotope values for Hodr vent are $\delta^{13}\text{C}_{\text{CH}_4} = -11.1\text{‰}$ and $\delta^{13}\text{C}_{\text{CO}_2} = -5.4\text{‰}$. The isotopic values of the bubble sample, $\delta^{13}\text{C}_{\text{CH}_4} = -8.1\text{‰}$ and $\delta^{13}\text{C}_{\text{CO}_2} = -1.7\text{‰}$, were more positive when compared with the Hodr fluid sample. The $^3\text{He}/^4\text{He}$ values in the Hodr pinnacle vent and Lily mound were $7.8 \text{ R/Ra}_{\text{corr}}$ and $8.6 \text{ R/Ra}_{\text{corr}}$, respectively. Similarly, the bubbles near Lily mound had a $^3\text{He}/^4\text{He}$ value of $8.6 \text{ R/Ra}_{\text{corr}}$. Prior to end-member calculation ($\text{Mg} = 0$), the lowest Mg concentration found was 1.6 mmol/L in the sample from the phase-separated vent, indicative of a reasonably pure end member sampling.

Table 6. Vent fluid (end-member) and gas compositions sampled from the Hodr pinnacle top, from phase separating fluids of Lily mound, and from bubbles escaping from surface fractures near Lily mound, Seven Sisters hydrothermal system.

Area		Hodr Pinnacle Top Hydrothermal Fluid		Lily Mound Hydrothermal Fluid		Seawater ¹
Depth		141 m		133 m		
Temp.		181 °C		200 °C		
Bottle		BL1		BL1	BL2	
pH		4.98		5.03	4.89	7.8
Alk	meq/l	0.25		0.04	0.04	2.4
Br	mmol/L	0.69		0.76	0.76	0.8
SO ₄	mmol/L	0.13		0.12	0.21	28
H ₂ S	μM	303.21		114.89	126.71	0
NH ₄	μM	51.80		57.73	56.91	0
NO ₂ ⁺³	μM	n.d.		n.d.	n.d.	
PO ₄	μM	1.43		1.56	1.53	
		<i>Filtered</i>	<i>Unfiltered</i>			
Na	mmol/L	381.98	371.13	393.37	393.11	464
K	mmol/L	34.55	34.69	37.41	37.38	10.1
Mg	mmol/L	-	-	-	-	52.2
Ca	mmol/L	40.80	40.97	43.57	43.38	10.2
Si	mmol/L	7.34	7.45	7.89	7.82	0.03–0.18
Mn	μmol/L	36.16	29.58	37.33	36.66	<0.001
Fe	μmol/L	11.69	13.45	7.12	7.33	<0.1
Sr	μmol/L	162.23	161.29	173.57	173.87	87
B	μmol/L	648.36	620.54	662.35	661.91	415
Li	μmol/L	n.d.	n.d.	n.d.	n.d.	26
Ba	μmol/L	31.03	22.47	97.12	102.11	0.14
Cr	nmol/l	n.d.	152.02	123.95	207.56	
Co	nmol/l	0.94	0.55	0.25	0.22	0.03
Ni	nmol/l	31.18	9.98	9.55	9.00	12
Cu	nmol/l	0.66	10.63	1.40	1.90	7
Zn	nmol/l	139.66	206.03	1727	2372	12
As	nmol/l	449.43	274.24	361.55	315.00	
Pb	nmol/l	0.06	9.19	0.04	0.16	0.01
Bottle		ROV15-GT16		ROV18-GT16		ROV16-GT17
Obs.		<i>Measured</i>	<i>End-Member</i>	<i>Measured</i>	<i>End-Member</i>	Near Lily
Mg	mmol/L	7.9	0	1.6	0	130 m
Cl	mmol/L	529	526	586	587	Gas bubble
Total Gas	mmol/kg	10.32	5.1*	3.01	3.01	%
CO ₂	mmol/kg	5.08	5.58	2.92	2.94	80.3
CH ₄	mmol/kg	0.01	0.02	0.03	0.03	4.31
H ₂	mmol/kg	0.004	0.004	0.008	0.009	0.010
Ne	mmol/kg	0.0001		0.0002		
N ₂	mmol/kg	3.611		0.13		14.8
O ₂	mmol/kg	1.344		0.03		
Ar	mmol/kg	0.075		0.002		
δ ¹³ CO ₂	‰ VPDB	−5.0	−5.4	n.d.	n.d.	−1.7
δ ¹³ CH ₄	‰ VPDB	−11.1	−11.1	n.d.	n.d.	−8.1
³ He/ ⁴ He	R/Ra corr		7.83		8.61	8.6

¹ seawater, [59].

5. Discussion

Shallow (<200 mbsl) submarine hydrothermal systems venting relatively high temperature (150–200 °C) fluids are uncommon at MOR settings [60,61]. Most known examples are located along arc, commonly proximal to sub-aerial volcanic islands [21,61–63]. Along the Mid-Atlantic Ridge, within a

ridge-hotspot setting, a few shallow hydrothermal systems have been identified. For example, near the Azores, shallow venting has been reported from the D. João de Castro bank, which is characterized by low-temperature (27–64 °C) degassing of volatile-rich fluids within bacterial mats [64,65]. Near Iceland, the shallow Eyjafjörður system discharges low to moderate (60–72 °C) temperature fluids through rare smectite chimney cones [66]. Along the Kolbeinsey ridge and south of Kolbeinsey Island, shallow venting (~110 mbsl) and moderate temperature venting (<131 °C) have been reported by (Ólafsson et al., 1988); on a deeper (~400 mbsl) section of the southernmost Kolbeinsey ridge, 30 km offshore Grimsey Island, Hannington et al. (2001) discovered a new type of shallow, high-temperature (250 °C), actively boiling hydrothermal system forming massive anhydrite chimneys with pyrite-marcasite crusts.

5.1. Explosive Volcanism, Mafic-Volcaniclastic Successions, and Hydrothermal Activity

The Seven Sisters hydrothermal system sits on one of the flat-topped, N–S aligned shallow volcanic edifices and likely originates from the same magmatic source as the adjacent summit caldera, known as the Eggvin Bank. These flat-topped volcanoes are probably cogenetic, erupting from a dike-like structure or/and from a single magma lens. The Seven Sister's proximity to Eggvin Bank, combined with extensive volcanism within the surrounding areas, is characteristic of relatively high magma supply [33]. Fresh, mafic, and highly vesicular basaltic scoria sampled from the flat-topped volcano that hosts the Seven Sisters magmatic-hydrothermal system indicates recent pre- to syn-eruptive degassing of exsolving volatiles in magma that was readily quenched at the seafloor. However, the most common volcanic lithotype is unconsolidated and consolidated volcanoclastic material that is ubiquitously distributed throughout the Seven Sisters site and that shows different grain-size distribution ranging from predominantly fine-ash to the north (e.g., Figure 4a), to coarse, 6 mm lapilli-tuff to the east. These volcanoclasts are evidence of episodic and explosive volcanism with load compaction of hot plastic glass (e.g., [67]), while their polymictic nature indicates some degree of post-depositional reworking. Explosive disruption of vesicles makes glass shards very susceptible to alteration so that the non-altered character of some samples suggests recent explosive volcanism. The laminated appearance of the consolidated deposit is the result of layers of partially oxidized material, indicative of seafloor weathering prior to further episodic explosive events, leading to the deposition of a new layer of glass shards.

At Seven Sisters, hydrothermal activity is pervasive on top of the volcanic edifice, either as diffuse venting with gas seeping through fractures covered by bacterial mats, bubbles seeping through the seafloor or, as focused, up to 200 °C venting from the clusters of craters, mounds, or pinnacle-like structures. The latter differs from a typical vent chimney as they are made up of products of vuggy barite-silica-pyrite and lack a well-defined central venting orifice. Similar structures have been observed at the Giggenbach and Clark volcanoes of the Kermadec Arc [68].

In ancient volcanoclastic-dominated VMS deposits, the diffuse discharge of hydrothermal fluids through permeable volcanoclastics, eventually capped by a silicified horizon, resulted in sulfide mineralization occurring by replacement, infilling pore spaces, and producing tabular subseafloor VMS deposits [69]. Under shallow-water, some of these volcanoclastic-dominated VMS deposits may be characterized by transitional features between VMS and epithermal deposits (e.g., aluminum-silicate or K-bearing alteration assemblages) [69,70]. Similarly, at Seven Sisters, seafloor venting of Ba- and Si-rich hydrothermal fluids in a non-consolidated, reworked, volcanoclastic deposit ensured rapid precipitation of barite (Figure 4f; [71]) and silica when the hydrothermal fluid mixes with seawater with concomitant sealing and insulation of the top layer. At Seven Sisters, the volcanoclastic-dominated lithologies are mafic in composition, making this a relatively unique shallow, mafic, volcanoclastic-hosted seafloor hydrothermal system.

5.2. Fluid Chemistry and Phase Separation Processes in a Shallow System

Fluid–rock interaction and phase separation can control vent fluid chemistry, resulting in a wide range in end-member compositions. This is particularly true in shallow systems, regardless of the

setting, where lower pressures (and temperature) promotes boiling, which in turn exerts a strong control on nature of metals to be transported in solution (e.g., [72]). Thus, metals that are transported at relatively lower temperatures, such as Ag, Au, As, Sb, Hb, Tl, Pb and Zn, tend to precipitate at shallower depths and above boiling zones [63], making shallow hydrothermal systems favorable settings for the precipitation of sulfides and sulfosalts containing these elements.

During phase separation (boiling), most elements are conservative relative to Cl, whereas dissolved gases (e.g., CO₂, CH₄, He, H₂, and H₂S) that do not form chloro-complexes segregate preferentially into the low Cl phase, that is, the vapor phase [59,73,74]. Changes in element ratios with respect to Cl provide information on the extent of the water–rock interaction (e.g., [58]). Fluids expelled from the Hodr pinnacle contain lower chlorinity and higher gas contents, suggesting that phase separation occurs beneath the structure. Moreover, low Na/Cl and high Ca/Cl and K/Cl values for these same vent fluids are indicative of Na uptake and Ca and K release reactions subseafloor. The depth (~130 m) and temperature (~200 °C) at which Lily mound fluids were sampled places them on the two-phase boundary for seawater (e.g., [75–77]), confirmed by the “flaming” effect caused by phase-separation processes recorded by the ROV cameras (Video S1).

Phase separation is an important mechanism for sulfide precipitation owing to cooling by decompression and an increase in pH and *f*O₂ following the loss of gas [78], which will physically limit venting temperatures [79], thus simultaneously influencing the metal transport capacity in the vapor and fluid phases [80–82]. Not surprisingly, the Seven Sisters vent fluids are metal-depleted when compared with a typical 1500–2500 m deep, higher temperature system (e.g., [20,55,77,83]). Nevertheless, fluids with relatively high Zn concentrations (200x that of seawater) vent from the mound. Arsenic found in Seven Sisters fluids ranges from 315 to 493 nmol/l, higher than As found in fluids from the Mid-Atlantic Ridge vent fields (<319 nmol/l) [84]. Vent fluids with higher As values have to our knowledge only been reported from hydrothermal systems in back-arc environments such as the Lau Basin [84].

5.3. Silica and Secondary Alteration Minerals

In shallow magmatic-hydrothermal systems, acid leaching alters feldspars producing kaolinite under low temperatures (<120 °C), and dickite at higher temperatures (150–350 °C) [85–88], making this assemblage, along with the presence of native sulfur, a key indicator of solutions with low pH [89]. Gangue minerals such as kaolinite-group minerals and vuggy silica were found at Seven Sisters, especially in the extensively altered volcanoclastic material. Similar alteration mineralogy has been previously described in seafloor hydrothermal systems associated to arc and back-arc settings (e.g., [16,20,90]).

Cryptocrystalline and microcrystalline silica phases are abundant at Seven Sisters, occurring either as sinter-like Si-crusts (containing Ag-Pb), or as a late-stage phase in volcanoclastic breccias mantling dendritic sulfides and sulfosalts. Late-stage filamentous spherules of cryptocrystalline silica and similar amorphous silica materials have also been described in submarine arc, back-arc, and MOR hydrothermal systems [50,91–96]. Under hydrothermal conditions, silica solubility decreases with decreasing temperature and pH, thus supersaturation and precipitation of silica occur preferentially by cooling prior to mixing with seawater [96–100]. At Seven Sisters, the lowest ⁸⁷Sr/⁸⁶Sr values (i.e., indicative of minimal mixing with seawater) correspond to these sinter-like materials (Table 3; Figure 6), consistent with a relatively pure end-member mineralizing fluid that leads to silica precipitation.

At 130 m water depth, boiling occurs at ~200 °C [75]. Cooling and supersaturation of silica and formation of silica colloids requires an initial fluid that is in equilibrium with quartz deeper in the system, at higher temperatures [94]. Fluids at Seven Sisters show relatively high dissolved Si (7–8 mmol/kg) for venting at ~13 bar and ~200 °C. By comparison, silica solubility calculated for seawater at ~150 bar and 200 °C is 4.56 mmol/kg [101]. Estimated minimum subseafloor reaction temperatures using the Fe/Mn geothermometer of [102] give a temperature range between 250 °C for Lily mound and 283 °C for the Hodr pinnacle. Assuming SiO₂ saturation at depth, the silica solubility

would be ~7.9 mmol/kg at 150 bar and 250 °C [101], a value that is similar to those observed at Seven Sisters. Although considered unlikely, subsurface mixing with a lower temperature fluid in equilibrium with amorphous silica [101] and low water/rock ratios [103] could also contribute to higher Si contents.

5.4. Magmatic Degassing at Seven Sisters

Magma degassing is the likely source of CO₂ in the Seven Sisters vent fluids. Carbon dioxide is predominant over other gas species found in the volatile fraction (Table 6). Saturation of dissolved CO₂ is about 5 mmol/kg at the depth, temperature, and salinity conditions found at Seven Sisters. Therefore, the formation and venting of CO₂-rich bubbles (>80% CO₂) near Lily mound suggest CO₂ concentrations greater than the solubility at 130 m water depth and a release of additional CO₂ to the gas phase.

The Hodr vent fluid $\delta^{13}\text{C}_{\text{CO}_2}$ value of -5.4‰ falls in the range of sediment-starved hydrothermal systems, commonly ascribed to a mantle carbon source [104,105]. Furthermore, R/Ra values derived from $^3\text{He}/^4\text{He}$ measurements for the Seven Sisters vent fluids have MORB-like signatures, again consistent with a mantle source (e.g., [106]). A $\delta^{13}\text{C}_{\text{CO}_2}$ value of -1.7‰ for the CO₂-rich bubbles venting near Lily mound appears too high to have a mantle-only source and likely reflects additional process(es) contributing to the bubble carbon budget. High $\delta^{13}\text{C}_{\text{CO}_2}$ fluids found in hydrothermal systems have been explained by either magma source enrichment due to slab-derived carbonate inputs (e.g., [7,104]) and/or degassing related to fractionation during early stages of CO₂ exsolution [107,108]. As degassing progresses, both exsolved CO₂ and residual melt become increasingly depleted in ^{13}C [107,109]. Carbonate input seems unlikely in this setting. On the other hand, magma resupply and degassing appear to be an episodic event within the Seven Sisters volcanic complex. We suggest, therefore, that the $\delta^{13}\text{C}_{\text{CO}_2}$ signature in the venting bubbles near Lily mound could indicate direct volatile exsolution from a relatively undegassed magma and that the Hodr fluids tap a mixture between that and reservoir equilibrated volatiles.

Both CH₄ and H₂ concentrations were low compared with other vent fields along the Mid-Atlantic Ridge, suggesting the hydrothermal system at Seven Sisters has not particularly interacted with sediments [47,110]. This is consistent with in situ pyrite sulfur isotope data (Figure 6), where the $\delta^{34}\text{S}$ values ($\sim 0.36\text{‰}$) cluster around MORB values precluding interaction of bacterially-reduced (i.e., low $\delta^{34}\text{S}$) sulfur from marine sediments [111].

Conversely, the Seven Sisters $\delta^{13}\text{C}_{\text{CH}_4}$ values are relatively high (-11.1‰ to -8.1‰) compared with sediment-starved, basalt-hosted hydrothermal vent systems [112]. The isotopic composition of CH₄ precludes a biogenic or thermogenic source for the excess CH₄ in the bubbles, and falls in a range typically observed in ultramafic environments originating from abiogenic contributions to the CH₄ budget [113], or favoring a process of reduction of mantle CO₂ [114,115]. An ultramafic input to the hydrothermal system at Seven Sisters would seem unlikely based on the geological setting. Notwithstanding, high $\delta^{13}\text{C}_{\text{CH}_4}$ values at Lucky Strike hydrothermal vent field of the Mid-Atlantic Ridge have been attributed to serpentinization of distal ultramafics [116]. It is more likely that subseafloor CH₄ oxidation [117] is the process responsible for the isotopic compositions values at Seven Sisters, which would be consistent with the mineralogical observations described above.

5.5. Tracing the Fluid Source at Seven Sisters

Barite is a common gangue mineral in the walls of vent chimneys where extensive mixing of seawater occurs (e.g., [16,94,96,118,119]). At Seven Sisters, ubiquitous barite is the first hydrothermal mineral to precipitate and is the dominant sulfate that builds up the venting structures (pinnacles and mounds), whereas anhydrite is less common and mostly associated with larger grain size volcanoclastic deposits (e.g., Figure 3F). Barite appears dispersed in silica, similarly reported in other shallow submarine hydrothermal vents [120] or as rosettes, and is common within mineralization at Brothers, Clark, and Rumble II West volcanoes of the Kermadec arc, where it is considered indicative of rapid precipitation and/or quenching [20,68,71,119].

Strontium and Ba are efficiently leached from basalts by hydrothermal fluids [103,121], with barite (which contains Sr) precipitating when seawater SO_4^{2-} mixes with Ba^{2+} carried by the hydrothermal fluid [94,122]. Consequently, the isotopic signature of $^{87}\text{Sr}/^{86}\text{Sr}$ in barite is a useful tool in identifying the fluid source [7,123,124]. At Kolbeinsey Ridge, seawater has a $^{87}\text{Sr}/^{86}\text{Sr}$ value of 0.709225 [51], while basalts sampled nearby at $\sim 71^\circ\text{N}$ (i.e., in close proximity to Seven Sisters) are less radiogenic with $^{87}\text{Sr}/^{86}\text{Sr} = 0.703047$ [48]. The average $^{87}\text{Sr}/^{86}\text{Sr}$ value for Seven Sisters is ~ 0.704340 , close to the isotope signature of local basalt, implying limited interaction with seawater by the hydrothermal fluids (Figure 6a).

The relative contribution of each endmember fluid that leads to barite precipitation can be assessed using a two component mixing model [125]:

$$\% \text{HF} = 100 \times \frac{[\text{Sr}]_{\text{SW}} [(^{87}\text{Sr}/^{86}\text{Sr})_{\text{SW}} - (^{87}\text{Sr}/^{86}\text{Sr})_{\text{M}}]}{[\text{Sr}]_{\text{HF}} [(^{87}\text{Sr}/^{86}\text{Sr})_{\text{M}} - (^{87}\text{Sr}/^{86}\text{Sr})_{\text{HF}}]} + \quad (1)$$

where $[\text{Sr}]_{\text{SW}}$ and $[\text{Sr}]_{\text{HF}}$ correspond to Sr concentrations in seawater and hydrothermal fluid (Table 6), and $(^{87}\text{Sr}/^{86}\text{Sr})_{\text{SW}}$, $(^{87}\text{Sr}/^{86}\text{Sr})_{\text{M}}$, and $(^{87}\text{Sr}/^{86}\text{Sr})_{\text{HF}}$ are the Sr-isotope ratios for seawater [51], barite-rich material (Table 3), and MOR-type hydrothermal fluid [126], respectively. The results support a predominant hydrothermal contribution of Sr ($\sim 67\% \pm 6\%$) over seawater ranging from 56% in the mineralized breccia to 74% in the silica-crust material.

Values of $\delta^{34}\text{S}$ in barite separates are wide-ranging and deviate from seawater (Figure 6a), whereas values $\delta^{34}\text{S}$ in pyrite are close to 0‰ (Figure 6b). Sulfide sulfur in unsedimented MOR settings ($\delta^{34}\text{S} \sim 1\text{‰} - 5\text{‰}$) originates mainly from the leaching of basaltic sulfide ($\delta^{34}\text{S} \sim 0\text{‰}$) by seawater derived sulfur ($\delta^{34}\text{S} \sim 21\text{‰}$), although additional sulfur contributions may occur from the interaction with sulfate-reducing bacteria and/or sediments, phase separation, and magmatic SO_2 [127].

Hydrogen sulfide produced by bacterial sulfate reduction is characterized by high $\Delta^{33}\text{S}$ and significantly negative and heterogeneous $\delta^{34}\text{S}$ [53,128–132]. We suggest that near-zero homogeneous $\delta^{34}\text{S}$ and slightly negative $\Delta^{33}\text{S}$ in pyrite (Figure 6b) is not compatible with significant biogenic sulfate reduction in the hydrothermal system. Furthermore, oxidation of H_2S during phase separation leads to considerable isotopic heterogeneity [133] that is not seen here, suggesting that disproportionation of magmatic SO_2^- [134] may be a contributing factor for the $\delta^{34}\text{S}$ values measured in Seven Sisters. Similar observations were made for the Hina Hine system in Lau Basin [135] and several arc volcano systems. Magmatic SO_2 disproportionates to H_2SO_4 , H_2S , and S during phase separation (e.g., [16,20]) with co-precipitation of sulfate minerals, sulfides, and native sulfur ensuring significant isotope fractionation between H_2SO_4 that is enriched in ^{34}S , and H_2S and S_0 that are depleted in ^{34}S (e.g., [134,136]). Moreover, the presence of elemental sulfur infilling vugs (Figure 3e) has been cited as evidence for condensation of magmatic SO_2 in association with characteristic magmatic-hydrothermal mineral assemblages [16,17,137].

5.6. Age of Mineralization

Recent barite mineralization true ages were determined using $^{228}\text{Th}/^{228}\text{Ra}$ values and range from 3.6 to 8.1 yr from the time of sampling (Table 5). These ages relate to samples taken from the top of actively venting pinnacles and mound.

The oldest barite mineralization events were estimated using $^{226}\text{Ra}/\text{Ba}$ values with minimum ages of 4840 and 4670 yr attributed to the Si-crust and base of Baldr pinnacle, respectively. Initial $^{226}\text{Ra}/\text{Ba}$ values for barite mirror the initial abundance of ^{226}Ra and Ba in the source rock; however, ascending hydrothermal fluids that transport the newly extracted Ba (and Ra) may dissolve and remobilize older seafloor barite (with ^{226}Ra that has already decayed), lowering the initial $^{226}\text{Ra}/\text{Ba}$ values [42,44,68]. Thus, when dating older barite components, comparing their $^{226}\text{Ra}/\text{Ba}$ values with the maximum $^{226}\text{Ra}/\text{Ba}$ values (i.e., the initial value used for the site) will give minimum ages rather than absolute ages [44].

Barite remobilization concomitant to zone refining processes in mounds and at the subsurface has been described in modern seafloor hydrothermal systems and their ancient VMS analogs (e.g., [43,44,52,68,96]). The observed multi-stage barite growth, if sourced by the remobilization of older barite from the mound and subsurface, may explain the observed wide range of $^{226}\text{Ra}/\text{Ba}$ values and ages at Seven Sisters (Table 5). To validate this assumption, radium isotope activities are decay-corrected, using ages derived from $^{228}\text{Th}/^{228}\text{Ra}$ values, to the time of mineralization for a $^{226}\text{Ra}/\text{Ba}$ versus $^{228}\text{Ra}/\text{Ba}$ mixing line (Figure 7). If barite was produced by separate hydrothermal events, the mixing line will intercept the $^{226}\text{Ra}/\text{Ba}$ axis, that is, give the $^{226}\text{Ra}/\text{Ba}$ value for the older barite component (Figure 7). Its age can then be calculated by comparison with the highest $^{226}\text{Ra}/\text{Ba}$ value, $49.1 \pm 0.5 \text{ Bq}\cdot\text{g}^{-1}$, taken as the initial value for mineralization containing minimal remobilized older barite (Table 5).

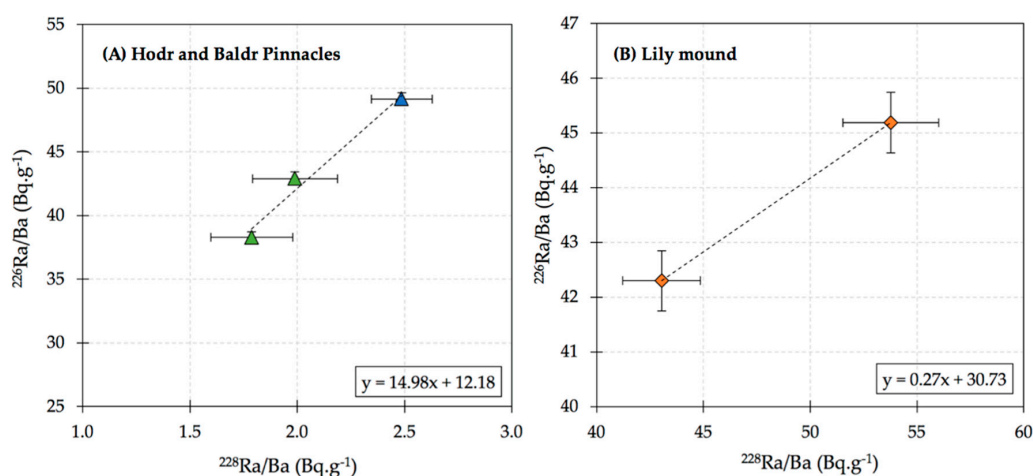


Figure 7. Plots showing the mixing line between recent barite (^{228}Ra and ^{226}Ra) and remobilized old barite (^{226}Ra only) in mineralized rocks the from Seven Sisters hydrothermal system. (A) Active Hodr and Baldr pinnacles; (B) active, phase-separating Lily mound.

From Figure 7a, the $^{226}\text{Ra}/\text{Ba}$ value for the older barite in the pinnacles is $12.2 \text{ Bq}\cdot\text{g}^{-1}$, which gives an age of $3220 \pm 560 \text{ yr}$, and is thus younger than the age estimated for the base of Baldr pinnacle (GS14ROV14R4) of $4670 \pm 60 \text{ yr}$. The large error (1σ) relates to the counting statistics on the relatively low ^{228}Ra activities and the decay corrections to the time of mineralization. The difference in age may be real considering GS14ROV14R4 is 75 m away from GS14ROV14R3 (Baldr Pinnacle), assuming that using data from both pinnacles for the mixing line is valid. The results for Lily mound samples GS14ROV15R1 and GS14ROV15R2 are more reliable owing to smaller errors. From Figure 7b, the $^{226}\text{Ra}/\text{Ba}$ value for the older barite is $30.7 \text{ Bq}\cdot\text{g}^{-1}$, which gives an age of $1080 \pm 270 \text{ yr}$, which is comparable to $1200 \pm 40 \text{ yr}$ for sample GS14ROV15R5, which is close ($<70 \text{ m}$) to the mound. The consistent ages derived by these different methods, that is, via the barite mixing line and by comparing the minimum and maximum $^{226}\text{Ra}/\text{Ba}$ values for the mound suite of samples, are evidence that the sample close to Lily mound is genuinely much younger than that of the base of Baldr pinnacle located $\sim 320 \text{ m}$ away (Figure 2e). Sample GS14DR2R2, a dredged Si-crust, is similar in age (4840 ± 70) to the base of Baldr pinnacle (Table 5).

5.7. A Shallow, Mafic Volcaniclastic Hosted VMS Analogue?

The spatial proximity between some subaerial epithermal and submarine VMS deposits raises the possibility that hybrid VMS deposits with epithermal-style mineralization may occur in shallow waters [70,138]. Shallow submarine hot springs are common in submerged volcanoes on island arcs with known porphyry copper and epithermal gold (e.g., [21,94,139–141]). In submarine settings, however, while high sulfidation and acid-sulfate alteration is common, seawater replaces meteoric water diluting magmatic derived fluids, buffering pH and temperature [70]. One example is the

submarine Brothers volcano, where the alteration mineral assemblages suggest a progression from an initially magmatically influenced to a seawater-dominated hydrothermal system [17]. At Brothers, the presence of illite, natroalunite, pyrophyllite, quartz, opal CT, pyrite, and native sulfur indicates high temperature reactions with acid-sulfate fluids. Sinter alteration, common in low-sulfidation deposits and neutral pH hot springs carrying Ag, Hg, Tl, Sb and Au [142], may actually occur in these seawater-buffered systems. The occurrence of these elements has been documented in some VMS deposits and resulted from condensation of ascending magmatic volatiles exsolved during boiling and oxidation of excess S in solution [2,143,144].

Sulfides are not abundant in the Seven Sisters surface samples and typically represent less than 10% of the mineralized rocks; nevertheless, for such minor sulfide abundance, whole-rock data shows relatively high contents for the ‘epithermal suite’ elements of Hg, Sb, Tl, Ag, Au and Mo (Table 2; Figure 8).

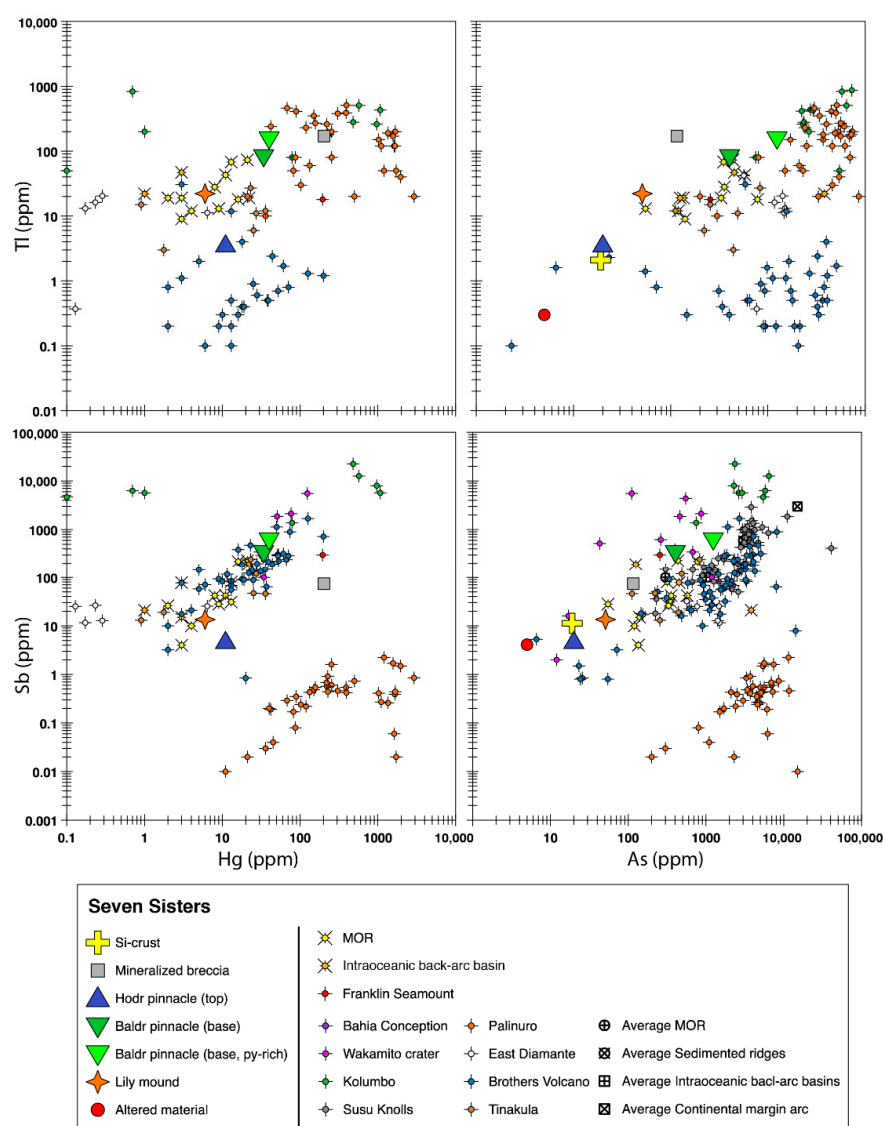


Figure 8. Epithermal suite element concentration of Seven Sisters rocks compared with equivalent samples from known seafloor hydrothermal systems with similarly high Tl, Hg, As, and Sb contents. Data source: MOR, intraoceanic back-arc basin, Franklin seamount sites [4], Bahia Conception [120], Brothers volcano [16], Wakamito crater [72], Kolumbo [22], Susu Knolls [145], Tinakula [146], and average values [147].

Pyrite-rich samples at Seven Sisters are enriched in Tl, Hg, As and Sb and their contents are comparable to those of magmatic-hydrothermal systems like Palinuro (for Tl) and Brothers volcano (for Sb) [16,21] (Figure 8). Few MORB samples also show comparable amounts of Tl (Figure 8) [4], although these samples are considerably more sulfide-rich than their Seven Sisters counterparts, emphasizing the epithermal suite enrichment at Seven Sisters.

Seven Sisters is located in a slow spreading ridge, where volatile-rich basalts and explosive volcanism are genetically related to mineralization, although no secondary carbonate minerals were found. Mineralization temperatures >200 °C are within the epithermal range, whereas the presence of argillic alteration, sulfate-sulfide-sulfosalt assemblages (with Ag, As, Tl, Sb, and Hg), and native sulfur, when combined with S, Sr and $\delta^{13}\text{C}_{\text{CO}_2}$ isotopic data in rocks and fluids, is evidence for magmatic input into the hydrothermal system.

Slow to ultra-slow MORB settings like the Northern Kolbeinsey Ridge (NKR) are not expected to host this type of mineralization, although the authors of [138] had hypothesized that even tholeiitic basalt emergent from MORB or hot spots could possess underappreciated epithermal potential. We thus propose that the mineralization style at Seven Sisters displays hybrid characteristics between VMS and seawater-buffered epithermal deposits.

6. Conclusions

The Seven Sisters is the first known shallow, hybrid, seafloor hydrothermal system with epithermal-style mineralization that is hosted in mafic volcanoclastics on a slow spreading ridge. The northern Kolbeinsey ridge area near Seven Sisters is characterized by enhanced volatile-rich magmatic activity, multiple episodes of explosive volcanism, and formation of volcanoclastic deposits with post-depositional reworking.

At Seven Sisters, hydrothermal fluids percolate through permeable mafic volcanoclastic deposits precipitating sulfate-sulfide minerals by replacement and in-filling of pore spaces. Focused, phase-separating of clear fluids of ~ 200 °C seep through unique barite-rich pinnacle-like structures and mounds.

Barite is ubiquitous and replaced by pyrite, which is the first sulfide to form, followed by Zn-Cu-Pb-Ag bearing sulfides, sulfosalts, and silica. Sulfides are scarce, usually less than 10%, resulting in relatively low ($<0.1\%$) base-metal (Cu-Zn-Pb) concentrations. However, whole rock data show high contents of 'epithermal suite' elements such as Hg, Tl, Sb, Ag, Au and Mo. Gangue alteration mineralogy assemblages (e.g., dickite) are suggestive of a magmatic influence on the hydrothermal systems.

End member vent fluids show both lower and higher than seawater chlorinity, have a pH of ~ 5 , and are depleted in metals. Higher dissolved metal contents are found in the mound fluids, where phase separation visibly occurs at the seafloor. Conversely, lower dissolved Cl and H_2S , combined with low metal content at the Hodr vent, suggest here that phase separation occurs subsurface, where sulfides are believed to be precipitating.

Carbon dioxide is expelled as bubbles ($>80\%$ CO_2) near Lily mound, and CO_2 dominates the volatile fraction at Seven Sisters fluids, with $\delta^{13}\text{C}$ values of -5 per mil as evidence for magmatic degassing from a relatively undegassed reservoir. Low concentrations of CH_4 (<0.026 mmol/kg) and H_2 (<0.009 mmol/kg) are consistent with a sediment-free hydrothermal system at Seven Sisters, corroborated by $^3\text{He}/^4\text{He}$ between 7.8 and 8.6 (R/Ra corr.), which shows MORB-like signatures, indicating an upper mantle source.

MORB-like multiple sulfur isotopes in early pyrite indicate little input from reduced seawater sulfate or leached sediments with biogenic sulfide, whereas sulfate $\delta^{34}\text{S}$ in barite is explained by the precipitation from a fluid containing seawater sulfate mixed with a small portion of lower $\delta^{34}\text{S}$ derived from the oxidation of magmatic sulfur. $^{87}\text{Sr}/^{86}\text{Sr}$ values in barite-dominated samples are close to the isotope signature of local basalt and indicate little seawater input into the hydrothermal fluids. The least radiogenic sample found at Seven Sisters is an Si crust. This sample has more negative than

seawater $\delta^{34}\text{S}_{\text{SO}_4}$ values and is ^{228}Ra depleted, and may be closer to pristine hydrothermal fluids at the summit of the Seven Sisters.

Hydrothermal barite-rich deposits have been produced, albeit intermittently, at Seven Sisters for at least 4700 yr, which is critical for better understanding the hydrothermal activity and distribution of seafloor mineral deposits in this area.

Supplementary Materials: The following are available online at <http://www.mdpi.com/2075-163X/10/5/439/s1>, File S1: XRD data; Video S1: Video footage (ROV dives 16 and 18) of Lily mound area showing the venting area from which 200 °C “flaming” fluids were sampled and temperatures probed.

Author Contributions: Conceptualization, A.F.A.M.; methodology, A.F.A.M., D.L.R., T.B., C.E.J.d.R., R.G.D., A.D., I.H.T., I.O., M.D.L., M.J.W. and R.B.P.; original draft preparation, A.F.A.M. and C.E.J.d.R.; writing—review and editing, A.F.A.M., D.L.R., T.B., C.E.J.d.R., R.G.D., and R.B.P. All authors have read and agreed to the published version of the manuscript.

Funding: This research has been supported by the Research Council of Norway and the K.G. Jebsen Centre for Deep Sea Research. The New Zealand government provided funding for C. de R. and R.D. for this work. This is PMEL contribution 4822.

Acknowledgments: We thank the captain and the crew of the R/V G.O. SARS, ROV pilots Asgeir Steinsland (IMR), Frank J. Widme and Erik Kleppe (Argus Remote Systems), and AUV operators Ole Lorentzen and Sjur Linnestad (FFI) for their invaluable technical support at sea. We thank shipboard and shore-based technical and engineering staff Yuval Ronen, Irina Dumitru, Siv Dundas, and Hildegunn Almelid of the University of Bergen, Cédric Hamelin for valuable assistance with the dredge planning and dredge operations; Leigh Evans for assistance in the Helium Isotope lab; Thomas Abraham-James for reviewing the text; and Institute of Marine Research for assistance with acquisition of data.

Conflicts of Interest: The authors declare no conflict of interest.

References

1. Von Damm, K.L. Seafloor hydrothermal activity: Black smoker chemistry and chimneys. *Annu. Rev. Earth Planet.* **1990**, *18*, 173–204. [[CrossRef](#)]
2. Yang, K.; Scott, S.D. Magmatic fluids as a source of metals in seafloor hydrothermal systems. *Geophys. Monogr.* **2006**, *166*, 1–23.
3. Hannington, M. Volcanogenic Massive Sulfide Deposits. In *Treatise on Geochemistry*; Elsevier: Amsterdam, The Netherlands, 2014; pp. 463–488.
4. Hannington, M.D.; de Ronde, C.E.J.; Petersen, S. Sea-floor tectonics and submarine hydrothermal systems. In *Economic Geology 100th Anniversary Volume*; Society of Economic Geologists: Littleton, CO, USA, 2005; pp. 111–141.
5. Stanton, R. *Ore Elements in Arc Lavas*; Oxford Science Publications: Oxford, UK, 1994; Volume 29.
6. Scott, S.D. Submarine Hydrothermal Systems and Deposits. In *Geochemistry of Hydrothermal Ore Deposits*, 3rd ed.; Barnes, H.L., Ed.; Wiley: New York, NY, USA, 1997; pp. 797–876.
7. Reeves, E.P.; Seewald, J.S.; Saccocia, P.; Bach, W.; Craddock, P.R.; Shanks, W.C.; Sylva, S.P.; Walsh, E.; Pichler, T.; Rosner, M. Geochemistry of hydrothermal fluids from the PACMANUS, Northeast Pual and Vienna Woods hydrothermal fields, Manus Basin, Papua New Guinea. *Geochim. Cosmochim. Acta* **2011**, *75*, 1088–1123. [[CrossRef](#)]
8. Leybourne, M.I.; Schwarz-Schampera, U.; de Ronde, C.E.J.; Baker, E.T.; Faure, K.; Walker, S.L.; Butterfield, D.A.; Resing, J.A.; Lupton, J.E.; Hannington, M.D.; et al. Submarine Magmatic-Hydrothermal Systems at the Monowai Volcanic Center, Kermadec Arc. *Econ. Geol.* **2012**, *107*, 1669–1694. [[CrossRef](#)]
9. Bottinga, Y.; Javoy, M. MORB degassing: Bubble growth and ascent. *Chem. Geol.* **1990**, *81*, 255–270. [[CrossRef](#)]
10. Dixon, J.; Stolper, E. An experimental study of water and carbon dioxide solubilities in Mid-Ocean Ridge basaltic liquids. Part II: Applications to degassing. *J. Petrol.* **1995**, *36*, 1633–1646.
11. Rubin, K. Degassing of metals and metalloids from erupting seamount and mid-ocean ridge volcanoes: Observations and predictions. *Geochim. Cosmochim. Acta* **1997**, *61*, 3525–3542. [[CrossRef](#)]
12. Lilley, M.; Butterfield, D.; Lupton, J.; Olson, E. Magmatic events can produce rapid changes in hydrothermal vent chemistry. *Nature* **2003**, *422*, 878–881. [[CrossRef](#)]

13. Yang, K.; Scott, S.D. Magmatic degassing of volatiles and ore metals into a hydrothermal system on the modern sea floor of the Eastern Manus Back-Arc Basin, Western Pacific. *Econ. Geol.* **2002**, *97*, 1079–1100. [[CrossRef](#)]
14. Yang, K.; Scott, S.D. Possible contribution of a metal-rich magmatic fluid to a sea-floor hydrothermal system. *Nature* **1996**, *383*, 420–423. [[CrossRef](#)]
15. Marques, A.F.A.; Scott, S.D.; Guillong, M. Magmatic degassing of ore-metals at the Menez Gwen: Input from the Azores plume into an active Mid-Atlantic Ridge seafloor hydrothermal system. *Earth Planet. Sci. Lett.* **2011**, *310*, 145–160. [[CrossRef](#)]
16. De Ronde, C.E.J.; Hannington, M.; Stoffers, P.; Wright, I.; Ditchburn, R.; Reyes, A.; Baker, E.; Massoth, G.; Lupton, J. Evolution of a Submarine Magmatic-Hydrothermal System: Brothers Volcano, Southern Kermadec Arc, New Zealand. *Econ. Geol.* **2005**, *100*, 1097–1133. [[CrossRef](#)]
17. De Ronde, C.E.J.; Humphris, S.E.; Höfig, T.W.; Reyes, A. IODP expedition. Critical role of caldera collapse in the formation of seafloor mineralization: The case of Brothers volcano. *Geology* **2019**, *47*, 762–766. [[CrossRef](#)]
18. Berkenbosch, H.A.; de Ronde, C.E.J.; Ryan, C.G.; McNeill, A.W.; Howard, D.L.; Gemmel, J.B.; Danyushevsky, L.V. Trace Element Mapping of Copper- and Zinc-Rich Black Smoker Chimneys from Brothers Volcano, Kermadec Arc, Using Synchrotron Radiation XFM and LA-ICP-MS. *Econ. Geol.* **2019**, *114*, 67–92. [[CrossRef](#)]
19. Stucker, V.K.; Walker, S.L.; de Ronde, C.E.J.; Tontini, F.C.; Tsuchida, S. Hydrothermal Venting at Hinepuia Submarine Volcano, Kermadec Arc: Understanding Magmatic-Hydrothermal Fluid Chemistry. *Geochem. Geophys. Geosyst.* **2017**, *18*, 3646–3661. [[CrossRef](#)]
20. Ronde, C.E.J.; Massoth, G.J.; Butterfield, D.A.; Christenson, B.W.; Ishibashi, J.; Ditchburn, R.G.; Hannington, M.D.; Brathwaite, R.L.; Lupton, J.E.; Kamenetsky, V.S.; et al. Submarine hydrothermal activity and gold-rich mineralization at Brothers Volcano, Kermadec Arc, New Zealand. *Miner. Depos.* **2011**, *46*, 541–584. [[CrossRef](#)]
21. Petersen, S.; Monecke, T.; Westhues, A.; Hannington, M.D.; Gemmel, J.B.; Sharpe, R.; Petters, M.; H., S.; Lackschewitz, K.S.; Augustin, N.; et al. Drilling shallow-water massive sulfides at the Palinuro Volcanic Complex, Aeolian Island Arc, Italy. *Econ. Geol.* **2014**, *109*, 2129–2157. [[CrossRef](#)]
22. Kiliyas, S.P.; Nomikou, P.; Papanikolaou, D.; Polymenakou, P.N.; Godelitsas, A.; Argyraki, A.; Carey, S.; Gamaletsos, P.; Mertzimekis, T.J.; Stathopoulou, E.; et al. New insights into hydrothermal vent processes in the unique shallow-submarine arc-volcano, Kolumbo (Santorini), Greece. *Sci. Rep.* **2013**, *3*, 2421. [[CrossRef](#)]
23. Glasby, G.; Lizasa, K.; Yuasa, M.; Usui, A. Submarine Hydrothermal Mineralization on the Izu-Bonin Arc, South of Japan: An Overview. *Mar. Georesources Geotechnol.* **2000**, *18*, 141–176. [[CrossRef](#)]
24. Hein, J.R.; Ronde, C.E.J.; Koski, R.; Ditchburn, R.G.; Mizzel, K.; Tamura, Y.; Stern, R.; Conrad, T.A.; Ishizuka, O.; Leybourne, M. Layered Hydrothermal Barite-Sulfide Mound Field, East Diamante Caldera, Mariana Volcanic Arc. *Econ. Geol.* **2014**, *109*, 2179–2206. [[CrossRef](#)]
25. Baker, E.T.; Embley, R.W.; Walker, S.L.; Resing, J.A.; Lupton, J.E.; Nakamura, K.-I.; de Ronde, C.E.J.; Massoth, G.J. Hydrothermal activity and volcano distribution along the Mariana arc. *J. Geophys. Res. Solid Earth* **2008**, *113*, B08S09. [[CrossRef](#)]
26. Hanert, H. Bacterial and chemical iron oxide deposition in a shallow bay on Palaea Kameni, Santorini, Greece: Microscopy, electron probe microanalysis, and photometry of in situ experiments. *Geomicrobiol. J.* **2002**, *19*, 317–342. [[CrossRef](#)]
27. Johnson, G.L.; Heezen, B.C. Morphology and evolution of the Norwegian-Greenland Sea. *Deep Sea Res.* **1967**, *14*, 755–771. [[CrossRef](#)]
28. Pedersen, R.B.; Thorseth, I.H.; Nygård, T.E.; Lilley, M.D.; Kelley, D.S. Hydrothermal Activity at the Arctic Mid-Ocean Ridges. In *Diversity of Hydrothermal Systems on Slow Spreading Ocean Ridges*; Rona, P., Devey, C.W., Dymont, J., Murton, B., Eds.; American Geophysical Union: Washington, DC, USA, 2010; pp. 67–89.
29. DeMets, C.; Gordon, R.G.; Argus, D.F. Geologically current plate motions. *Geophys. J. Int.* **2010**, *181*, 1–80. [[CrossRef](#)]
30. Pedersen, R.B.; Rapp, H.T.; Thorseth, I.H.; Lilley, M.D.; Barriga, F.J.A.S.; Baumberger, T.; Flesland, K.; Fonseca, R.; Früh-Green, G.L.; Jorgensen, S.L. Discovery of a black smoker vent field and vent fauna at the Arctic Mid-Ocean Ridge. *Nat. Comms.* **2010**, *1*, 1–6. [[CrossRef](#)] [[PubMed](#)]

31. Kodaira, S.; Mjelde, R.; Gunnarsson, K.; Shiobara, H.; Shimamura, H. Crustal structure of the Kolbeinsey Ridge, North Atlantic, obtained by use of ocean bottom seismographs. *J. Geophys. Res. Solid Earth* **1997**, *102*, 3131–3151. [[CrossRef](#)]
32. Appelgate, B. Modes of axial reorganization on a slow-spreading ridge: The structural evolution of Kolbeinsey Ridge since 10 Ma. *Geology* **1997**, *25*, 431–434. [[CrossRef](#)]
33. Tan, P.; Breivik, A.J.; Trønnes, R.G.; Mjelde, R.; Azuma, R.; Eide, S. Crustal structure and origin of the Eggvin Bank west of Jan Mayen, NE Atlantic. *J. Geophys. Res. Solid Earth* **2017**, *122*, 43–62. [[CrossRef](#)]
34. Yeo, I.A.; Devey, C.W.; LeBas, T.P.; Augustin, N.; Steinführer, A. Segment-scale volcanic episodicity: Evidence from the North Kolbeinsey Ridge, Atlantic. *Earth Planet. Sci. Lett.* **2016**, *439*, 81–87. [[CrossRef](#)]
35. Marques, A.F.A.; Pedersen, R.B.; Roerdink, D.; Baumberger, T.; Thorseth, I.H.; Hamelin, C.O.S.; Okland, I.; Stensland, A. Shallow water venting on the Arctic Mid-Ocean ridge: The Seven Sisters hydrothermal system. In *Mineral Resources in a Sustainable World*. In Proceedings of the 13th SGA Biennial Meeting, Nancy, France, 24–27 August 2015; Volume 3, pp. 1253–1256.
36. Fossum, T.G.; Saebo, T.O.; Langli, B.; Callow, H.; Hansen, R.E. HISAS 1030: High resolution synthetic aperture sonar with bathymetric capabilities. *Shallow Surv. Portsm. NH USA* **2008**, *10*, 11.
37. Hansen, R.E.; Saebo, T.O.; Callow, H.J.; Hagen, P.E.; Hammerstad, E. Synthetic aperture sonar processing for the HUGIN AUV. In *Europe Oceans*; IEEE: Piscataway, NJ, USA, 2005; Volume 2, pp. 1090–1094.
38. Whitehouse, M.J. Multiple Sulfur Isotope Determination by SIMS: Evaluation of Reference Sulfides for $\Delta 33S$ with Observations and a Case Study on the Determination of $\Delta 36S$. *Geostand. Geoanalytical Res.* **2013**, *37*, 19–33. [[CrossRef](#)]
39. Cabral, R.A.; Jackson, M.G.; Rose-Koga, E.F.; Koga, K.T.; Whitehouse, M.J.; Antonelli, M.A.; Farquhar, J.; Day, J.M.D.; Hauri, E.H. Anomalous sulphur isotopes in plume lavas reveal deep mantle storage of Archaean crust. *Nature* **2013**, *496*, 490–493. [[CrossRef](#)] [[PubMed](#)]
40. Roerdink, D.L.; Mason, P.R.D.; Whitehouse, M.J.; Brouwer, F.M. Reworking of atmospheric sulfur in a Paleoproterozoic hydrothermal system at Londozi, Barberton Greenstone Belt, Swaziland. *Precambrian Res.* **2016**, *280*, 195–204. [[CrossRef](#)]
41. Ditchburn, R.G.; Graham, I.J.; Barry, B.J. Uranium series disequilibrium dating of black smoker chimneys. *New Zealand Sci. Rev.* **2004**, *61*, 54–56.
42. Ditchburn, R.G.; de Ronde, C.E.J.; Barry, B.J. Radiometric Dating of Volcanogenic Massive Sulfides and Associated Iron Oxide Crusts with an Emphasis on Ra-226/Ba and Ra-228/Ra-226 in Volcanic and Hydrothermal Processes at Intraoceanic Arcs. *Econ. Geol.* **2012**, *107*, 1635–1648. [[CrossRef](#)]
43. Jamieson, J.W.; Hannington, M.D.; Tivey, M.K.; Hansteen, T.; Williamson, N.M.B.; Stewart, M.; Fietzke, J.; Butterfield, D.; Frische, M.; Allen, L.; et al. Precipitation and growth of barite within hydrothermal vent deposits from the Endeavour Segment, Juan de Fuca Ridge. *Geochim. Cosmochim. Acta* **2016**, *173*, 64–85. [[CrossRef](#)]
44. Ditchburn, R.G.; de Ronde, C.E.J. Evidence for Remobilization of Barite Affecting Radiometric Dating Using ^{228}Ra , ^{228}Th , and $^{226}Ra/Ba$ Values: Implications for the Evolution of Sea-Floor Volcanogenic Massive Sulfides. *Econ. Geol.* **2017**, *112*, 1231–1245. [[CrossRef](#)]
45. Lupton, J.; Butterfield, D.; Lilley, M.; Evans, L.; Nakamura, K.-I.; Chadwick, W.; Resing, J.; Embley, R.; Olson, E.; Proskurowski, G.; et al. Submarine venting of liquid carbon dioxide on a Mariana Arc volcano. *Geochem. Geophys. Geosyst.* **2006**, *7*, 08007. [[CrossRef](#)]
46. Mottl, M.J.; Holland, H.D. Chemical exchange during hydrothermal alteration of basalt by seawater—I. Experimental results for major and minor components of seawater. *Geochim. Cosmochim. Acta* **1978**, *42*, 1103–1115. [[CrossRef](#)]
47. Baumberger, T.; Früh-Green, G.L.; Thorseth, I.H.; Lilley, M.D.; Hamelin, C.; Bernasconi, S.M.; Okland, I.E.; Pedersen, R.B. Fluid composition of the sediment-influenced Loki's Castle vent field at the ultra-slow spreading Arctic Mid-Ocean Ridge. *Geochim. Cosmochim. Acta* **2016**, *187*, 156–178. [[CrossRef](#)]
48. Elkins, L.J.; Hamelin, C.; Blichert-Toft, J. North Atlantic hotspot-ridge interaction near Jan Mayen Island. *Geochem. Perspect.* **2016**, *2*, 55–67. [[CrossRef](#)]
49. Paytan, A.; Mearon, S.; Cobb, K.; Kastner, M. Origin of marine barite deposits: Sr and S isotope characterization. *Geology* **2002**, *30*, 747–750. [[CrossRef](#)]
50. Binns, R.A.; Parr, J.M.; Gemmel, J.B.; Whitford, D.J.; Dean, J.A. Precious metals in barite-silica chimneys from Franklin Seamount, Woodlark Basin, Papua New Guinea. *Mar. Geol.* **1997**, *142*, 119–141. [[CrossRef](#)]

51. Kuhn, T.; Herzig, P.M.; Hannington, M.D.; Garbe-Schönberg, D.; Stoffers, P. Origin of fluids and anhydrite precipitation in the sediment-hosted Grimsey hydrothermal field north of Iceland. *Chem. Geol.* **2003**, *202*, 5–21. [[CrossRef](#)]
52. Eickmann, B.; Thorseth, I.H.; Peters, M.; Strauss, H.; Bröcker, M.; Pedersen, R.B. Barite in hydrothermal environments as a recorder of seafloor processes: A multiple-isotope study from the Loki's Castle vent field. *Geobiology* **2014**, *12*, 308–321. [[CrossRef](#)]
53. Ono, S.; Shanks, W.C., III; Rouxel, O.J.; Rumble, D. S-33 constraints on the seawater sulfate contribution in modern seafloor hydrothermal vent sulfides. *Geochim. Cosmochim. Acta* **2007**, *71*, 1170–1182. [[CrossRef](#)]
54. Seyfried, W.E.J.; Pester, N.J.; Ding, K.; Rough, M. Vent fluid chemistry of the Rainbow hydrothermal system (36 degrees N, MAR): Phase equilibria and in situ pH controls on seafloor alteration processes. *Geochim. Cosmochim. Acta* **2011**, *75*, 1574–1593. [[CrossRef](#)]
55. Charlou, J.-L.; Donval, J.-P.; Douville, E.; Jean-Baptiste, P.; Radford-Knoery, J.; Fouquet, Y.; Dapigny, A.; Stievenard, M. Compared geochemical signatures and the evolution of Menez Gwen (37°50′N) and Lucky Strike (37°17′N) hydrothermal fluids, south of the Azores Triple Junction on the Mid-Atlantic Ridge. *Chem. Geol.* **2000**, *171*, 49–75. [[CrossRef](#)]
56. Von Damm, K.; Bray, A.; Buttermore, L.; Oosting, S. The geochemical controls on vent fluids from the Lucky Strike vent field, Mid-Atlantic Ridge. *Earth Planet. Sci. Lett.* **1998**, *160*, 521–536. [[CrossRef](#)]
57. De Ronde, C.E.J.; Stucker, V.K. Seafloor Hydrothermal Venting at Volcanic Arcs and Backarcs. In *The Encyclopedia of Volcanoes*, 2nd ed.; Sigurdsson, H., Ed.; Elsevier, Ltd.: Amsterdam, The Netherlands, 2015; pp. 823–849.
58. Von Damm, K.; Buttermore, L.; Oosting, S.; Bray, A.; Fornari, D.; Lilley, M.; Shanks, E., III. Direct Observation of the evolution of a seafloor “black smoker” from vapor to brine. *Earth Planet. Sci. Lett.* **1997**, *149*, 101–111. [[CrossRef](#)]
59. German, C.R.; Von Damm, K.L. Hydrothermal Processes. In *Treatise on Geochemistry*; Rudnick, R.L., Ed.; Elsevier, Ltd.: Amsterdam, The Netherlands, 2003; Volume 6, pp. 181–222.
60. Beaulieu, S.E.; Baker, E.T.; German, C.R.; Maffei, A. An authoritative global database for active submarine hydrothermal vent fields. *Geochem. Geophys. Geosyst.* **2013**, *14*, 4892–4905. [[CrossRef](#)]
61. Monecke, T.; Petersen, S.; Hannington, M.D. Constraints on water depth of massive sulfide formation: Evidence from modern seafloor hydrothermal systems in Arc-related settings. *Econ. Geol.* **2014**, *109*, 2079–2101. [[CrossRef](#)]
62. Yamanaka, T.; Maeto, K.; Akashi, H.; Ishibashi, J.-I.; Miyoshi, Y.; Okamura, K.; Noguchi, T.; Kuwahara, Y.; Toki, T.; Tsunogai, U.; et al. Shallow submarine hydrothermal activity with significant contribution of magmatic water producing talc chimneys in the Wakamiko Crater of Kagoshima Bay, southern Kyushu, Japan. *J. Volcanol. Geotherm. Res.* **2013**, *258*, 74–84. [[CrossRef](#)]
63. Hannington, M.D. Shallow Submarine Hydrothermal Systems and Associated Mineral Deposits (Preliminary Map); Geological Survey of Canada Open File Report 3421. 1999; Map 1:35,000,000.
64. Cardigos, F.; Colaço, A.; Dando, P.; Ávila, S.; Sarradin, P.-M.; Tempera, F.; Conceição, P.; Pascoal, A.; Serrão, S. Shallow water hydrothermal vent field fluids and communities of the D. João de Castro Seamount (Azores). *Chem. Geol.* **2005**, *224*, 153–168. [[CrossRef](#)]
65. Ólafsson, J.; Honjo, S.; Thors, K.; Stefánsson, U.; Jones, R.R.; Ballard, R.D. Initial observations, bathymetry and photography of a geothermal site on the Kolbeinsey Ridge. In *Oceanography 1988*; Ayala-Castañares, A., Wooster, W.A.Y.-A., Eds.; UNAM Press: Windhoek, Namibia, 1988; p. 208.
66. Marteinson, V.T.; Kristjánsson, J.K.; Kristmannsdóttir, H.; Dahlkvist, M.; Sæmundsson, K.; Hannington, M.; Pétursdóttir, S.K.; Geptner, A.; Stoffers, P. Discovery and Description of Giant Submarine Smectite Cones on the Seafloor in Eyjafjörður, Northern Iceland, and a Novel Thermal Microbial Habitat. *Appl. Environ. Microbiol.* **2001**, *67*, 827–833. [[CrossRef](#)]
67. McPhie, J.; Doyle, M.G.; Allen, R. *Volcanic Textures: A Guide to the Interpretation of Textures in Volcanic Rocks*; Centre for Ore Deposit and Exploration Studies (CODES), University of Tasmania: Hobart, Tasmania, 1993.
68. De Ronde, C.E.J.; Walker, S.L.; Ditchburn, R.G.; Tontini, F.C.; Hannington, M.D.; Merle, S.G.; Timm, C.; Handler, M.R.; Wysoczanski, R.J.; Dekov, V.M.; et al. The Anatomy of a Buried Submarine Hydrothermal System, Clark Volcano, Kermadec Arc, New Zealand. *Econ. Geol.* **2014**, *109*, 2261–2292. [[CrossRef](#)]

69. Gibson, H.L.; Morton, R.L.; Hudak, G. Submarine volcanic processes, deposits. In *Volcanic-Associated Massive Sulfide Deposits—Processes and Examples in Modern and Ancient Settings*; Barrie, C.T., Hannington, M.D., Eds.; Reviews in Economic Geology, Society of Economic Geologists: Littleton, CO, USA, 1999; pp. 13–51.
70. Hannington, M.D.; Poulsen, K.; Thompson, J.F.H.; Sillitoe, R.H. Volcanogenic gold in the massive sulfide environment Volcanic-associated massive sulfide deposits. *Rev. Econ. Geol.* **1999**, *8*, 325–356.
71. De Ronde, C.E.; Faure, K.; Bray, C.J.; Chappell, D.A.; Wright, I.C. Hydrothermal fluids associated with seafloor mineralization at two southern Kermadec arc volcanoes, offshore New Zealand. *Miner. Depos.* **2003**, *38*, 217–233. [[CrossRef](#)]
72. Ishibashi, J.-I.; Nakaseama, M.; Seguchi, M.; Yamashita, T.; Doi, S.; Sakamoto, T.; Shimada, K.; Shimada, N.; Noguchi, T.; Oomori, T.; et al. Marine shallow-water hydrothermal activity and mineralization at the Wakamiko crater in Kagoshima bay, south Kyushu, Japan. *J. Volcanol. Geotherm. Res.* **2008**, *173*, 84–98. [[CrossRef](#)]
73. Berndt, M.; Seyfried, W., Jr. Boron, bromine, and other trace elements as clues to the fate of chlorine in mid-ocean ridge vent fluids. *Geochim. Cosmochim. Acta* **1990**, *54*, 2235–2245. [[CrossRef](#)]
74. Von Damm, K.; Lilley, M.; Shanks, E., III; Brockington, M.; Bray, A.; O’Grady, K.; Olson, E.; Graham, A.; Proskurowski, G.; Party, S. Extraordinary phase separation and segregation in vent fluids from the Southern East Pacific Rise. *Earth Planet. Sci. Lett.* **2003**, *206*, 365–378. [[CrossRef](#)]
75. Bischoff, J.L.; Rosenbauer, R.J. The critical point and two-phase boundary of seawater, 200 °C–500 °C. *Earth Planet. Sci. Lett.* **1984**, *68*, 172–180. [[CrossRef](#)]
76. Bischoff, J.L.; Rosenbauer, R.J. Phase separation in seafloor geothermal systems; an experimental study of the effects on metal transport. *Am. J. Sci.* **1987**, *287*, 953–978. [[CrossRef](#)]
77. Von Damm, K.; Humphris, S.; Lupton, J.; Mullineaux, L.; Zierenberg, R. Controls on the chemistry and temporal variability of seafloor hydrothermal fluids. *Geophys. Monogr.* **1995**, *91*, 222–247.
78. Drummond, S.; Ohmoto, H. Chemical Evolution and Mineral Deposition in Boiling Hydrothermal Systems. *Econ. Geol.* **1985**, *80*, 126–147. [[CrossRef](#)]
79. Ohmoto, H. Formation of volcanogenic massive sulfide deposits: The Kuroko perspective. *Ore Geol. Rev.* **1996**, *10*, 135–177. [[CrossRef](#)]
80. Fouquet, Y.; Auclair, G.; Cambon, P.; Etoubleau, J. Geological setting and mineralogical and geochemical investigations on sulfide deposits near 13 °N on the East Pacific Rise. *Miner. Depos.* **1988**, *84*, 145–178. [[CrossRef](#)]
81. Hannington, M.; Herzig, P.; Scott, S.D.; Thompson, G.; Rona, P. Comparative mineralogy and geochemistry of gold-bearing sulfide deposits on the mid-ocean ridges. *Mar. Geol.* **1991**, *101*, 217–248. [[CrossRef](#)]
82. Herzig, P.M.; Hannington, M.D. Polymetallic massive sulfides at the modern seafloor—A review. *Ore Geol. Rev.* **1995**, *10*, 95–115. [[CrossRef](#)]
83. German, C.R.; Seyfried, W.E. Hydrothermal Processes. In *Treatise on Geochemistry*, 2nd ed.; Elsevier: Amsterdam, The Netherlands, 2013; Volume 8, pp. 191–233.
84. Douville, E.; Charlou, J.-L.; Donval, J.-P.; Hureau, D.; Appriou, P. Le comportement de l’arsenic (As) et de l’antimoine (Sb) dans les fluides provenant de différents systèmes hydrothermaux océaniques. *Comptes Rendus Académie Sci. Ser. IIA Earth Planet. Sci.* **1999**, *328*, 97–104.
85. Schroeder, R.J. Dickite and Kaolinite in Pennsylvanian Limestones of Southeastern Kansas. *Clays Clay Miner.* **1968**, *16*, 41–49. [[CrossRef](#)]
86. Zotov, A.; Mukhamet-Galeev, A.; Schott, J. An experimental study of kaolinite and dickite relative stability at 150–300 degrees C and the thermodynamic properties of dickite. *Am. Mineral.* **1998**, *83*, 516–524. [[CrossRef](#)]
87. Ehrenberg, S.N. Depth-Dependent Transformation of Kaolinite to Dickite in Sandstones of the Norwegian Continental Shelf. *Clay Miner.* **1993**, *28*, 325–352. [[CrossRef](#)]
88. Premović, P.; Ciesielczuk, J.; Bzowska, G.; Đorđević, M. Geochemistry and electron spin resonance of hydrothermal dickite (Nowa Ruda, Lower Silesia, Poland): Vanadium and chromium. *Geol. Carpathica* **2012**, *63*, 241–252. [[CrossRef](#)]
89. Einaudi, M.T.; Hedenquist, J.W.; Inan, E.E. Sulfidation state of fluids in active and extinct hydrothermal systems: Transitions from porphyry to epithermal environments. *Spec. Publ. Soc. Econ. Geol.* **2003**, *10*, 285–313.

90. Yeats, C.J.; Hollis, S.P.; Halfpenny, A.; Corona, J.-C.; LaFlamme, C.; Southam, G.; Fiorentini, M.; Herrington, R.J.; Spratt, J. Actively forming Kuroko-type volcanic-hosted massive sulfide (VHMS) mineralization at the Iheya North, Okinawa Trough. *Japan. Ore Geol. Rev.* **2017**, *84*, 20–41. [[CrossRef](#)]
91. Knott, R.; Fouquet, Y.; Honnorez, J.; Petersen, S.; Bohn, M. Petrology of hydrothermal mineralization: A vertical section through the TAG mound. In *Proceedings of the Ocean Drilling Program, Scientific Results*. 1998; Volume 158, 5–26.
92. Hopkinson, L.; Roberts, S.; Herrington, R.; Wilkinson, J. The nature of crystalline silica from the TAG submarine hydrothermal mound, 26°N Mid Atlantic Ridge. *Contrib. Mineral. Petrol.* **1999**, *137*, 342–350. [[CrossRef](#)]
93. Binns, R.A. Bikpela: A Large Siliceous Chimney from the PACMANUS Hydrothermal Field, Manus Basin, Papua New Guinea. *Econ. Geol.* **2014**, *109*, 2243–2259. [[CrossRef](#)]
94. Urabe, T.; Kusakabe, M. Barite silica chimneys from the Sumisu Rift, Izu-Bonin Arc: Possible analogue to hematitic chert associated with Kuroko deposits. *Earth Planet. Sci. Lett.* **1990**, *100*, 283–290. [[CrossRef](#)]
95. Koski, R.; Jonasson, I.R.; Kadko, D.C.; Smith, V.K.; Wong, F.L. Compositions, growth mechanisms, and temporal relations of hydrothermal sulfide-sulfate-silica chimneys at the northern Cleft segment, Juan de Fuca Ridge. *J. Geophys. Res. Solid Earth* **1994**, *99*, 4813–4832. [[CrossRef](#)]
96. Hannington, M.D.; Scott, S.D. Mineralogy and geochemistry of a hydrothermal silica-sulfide-sulfate spire in the caldera of Axial Seamount, Juan De Fuca Ridge. *Can. Mineral.* **1988**, *26*, 603–625.
97. Rodgers, K.A.; Browne, P.R.L.; Buddle, T.F.; Cook, K.L.; Greatrex, R.A.; Hampton, W.A.; Herdianita, N.R.; Holland, G.R.; Lynne, B.Y.; Martin, R.; et al. Silica phases in sinters and residues from geothermal fields of New Zealand. *Earth Sci. Rev.* **2004**, *66*, 1–61. [[CrossRef](#)]
98. Tivey, M.K.; Delaney, J.R. Growth of large sulfide structures on the endeavour segment of the Juan de Fuca ridge. *Earth Planet. Sci. Lett.* **1986**, *77*, 303–317. [[CrossRef](#)]
99. White, D.E.; Brannock, W.W.; Murata, K.J. Silica in hot-spring waters. *Geochim. Cosmochim. Acta* **1956**, *10*, 27–59. [[CrossRef](#)]
100. Janecky, D.R.; Seyfried, W., Jr. Formation of massive sulfide deposits on oceanic ridges: Incremental reaction models for mixing between hydrothermal solutions and seawater. *Geochim. Cosmochim. Acta* **1984**, *48*, 2723–2738. [[CrossRef](#)]
101. Von Damm, K.L.; Bischoff, J.L.; Rosenbauer, R.J. Quartz solubility in hydrothermal seawater; an experimental study and equation describing quartz solubility for up to 0.5 M NaCl solutions. *Am. J. Sci.* **1991**, *291*, 977–1007. [[CrossRef](#)]
102. Pester, N.J.; Rough, M.; Ding, K.; Seyfried, W.E., Jr. A new Fe/Mn geothermometer for hydrothermal systems: Implications for high-salinity fluids at 13°N on the East Pacific Rise. *Geochim. Cosmochim. Acta* **2011**, *75*, 7881–7892. [[CrossRef](#)]
103. Seyfried, W., Jr.; Mottl, M. Hydrothermal alteration of basalt by seawater under seawater-dominated conditions. *Geochim. Cosmochim. Acta* **1982**, *46*, 985–1002. [[CrossRef](#)]
104. Matthey, D.P.; Carr, R.H.; Wright, I.P.; Pillinger, C.T. Carbon isotopes in submarine basalts. *Earth Planet. Sci. Lett.* **1984**, *70*, 196–206. [[CrossRef](#)]
105. Pineau, F.; Javoy, M. Carbon isotopes and concentrations in mid-oceanic ridge basalts. *Earth Planet. Sci. Lett.* **1983**, *62*, 239–257. [[CrossRef](#)]
106. Lupton, J.; Rubin, K.H.; Arculus, R.; Lilley, M.; Butterfield, D.; Resing, J.; Baker, E.; Embley, R. Helium isotope, C/3He, and Ba-Nb-Ti signatures in the northern Lau Basin: Distinguishing arc, back-arc, and hotspot affinities. *Geochem. Geophys. Geosyst.* **2015**, *16*, 1133–1155. [[CrossRef](#)]
107. Javoy, M.; Pineau, F.; Iiyama, I. Experimental determination of the isotopic fractionation between gaseous CO₂ and carbon dissolved in tholeiitic magma. *Contrib. Mineral. Petrol.* **1978**, *67*, 35–39. [[CrossRef](#)]
108. Ishibashi, J.-I.; Wakita, H.; Nojiri, Y.; Grimaud, D.; Jean-Baptiste, P.; Gamo, T.; Auzende, J.-M.; Urabe, T. Helium and carbon geochemistry of hydrothermal fluids from the North Fiji Basin spreading ridge (southwest Pacific). *Earth Planet. Sci. Lett.* **1994**, *128*, 183–197. [[CrossRef](#)]
109. Matthey, D.P. Carbon dioxide solubility and carbon isotope fractionation in basaltic melt. *Geochim. Cosmochim. Acta* **1991**, *55*, 3467–3473. [[CrossRef](#)]
110. Baumberger, T.; Früh-Green, G.L.; Dini, A.; Boschi, C.; van Zuilen, K.; Thorseth, I.H.; Pedersen, R.B. Constraints on the sedimentary input into the Loki's Castle hydrothermal system (AMOR) from B isotope data. *Chem. Geol.* **2016**, *443*, 111–120. [[CrossRef](#)]

111. Seal, R.R., II. Sulfur Isotope Geochemistry of Sulfide Minerals. *Rev. Mineral. Geochem.* **2006**, *61*, 633–677. [[CrossRef](#)]
112. Tsunogai, U.; Yoshida, N.; Ishibashi, J.; Gamo, T. Carbon isotopic distribution of methane in deep-sea hydrothermal plume, Myojin Knoll Caldera, Izu-Bonin arc: Implications for microbial methane oxidation in the oceans and applications to heat flux estimation. *Geochim. Cosmochim. Acta* **2000**, *64*, 2439–2452. [[CrossRef](#)]
113. Konn, C.; Charlou, J.L.; Holm, N.G.; Mousis, O. The Production of Methane, Hydrogen, and Organic Compounds in Ultramafic-Hosted Hydrothermal Vents of the Mid-Atlantic Ridge. *Astrobiology* **2015**, *15*, 381–399. [[CrossRef](#)]
114. Welhan, J. Origins of methane in hydrothermal systems. *Chem. Geol.* **1988**, *71*, 183–198. [[CrossRef](#)]
115. Cruse, A.M.; Seewald, J.S. Low-molecular weight hydrocarbons in vent fluids from the Main Endeavour Field, northern Juan de Fuca Ridge. *Geochim. Cosmochim. Acta* **2010**, *74*, 6126–6140. [[CrossRef](#)]
116. Pester, N.J.; Reeves, E.P.; Rough, M.E.; Ding, K.; Seewald, J.S.; Seyfried, W.E., Jr. Subseafloor phase equilibria in high-temperature hydrothermal fluids of the Lucky Strike Seamount (Mid-Atlantic Ridge, 37°17'N). *Geochim. Cosmochim. Acta* **2012**, *90*, 303–322. [[CrossRef](#)]
117. Whiticar, M.J. Carbon and hydrogen isotope systematics of bacterial formation and oxidation of methane. *Chem. Geol.* **1999**, *161*, 291–314. [[CrossRef](#)]
118. Eickemann, B.; Baumberger, T.; Thorseth, I.H.; Strauss, H.; Früh-Green, G.L.; Pedersen, R.B.; Jaeschle, A. Sub-seafloor sulfur cycling in a low temperature barite field: A multi-proxy study from the Arctic Loki's Castle vent field. *Chem. Geol.* **2020**, *539*, 119495. [[CrossRef](#)]
119. Berkenbosch, H.A.; de Ronde, C.E.J.; Gemmill, J.B.; McNeill, A.W.; Goemann, K. Mineralogy and Formation of Black Smoker Chimneys from Brothers Submarine Volcano, Kermadec Arc. *Econ. Geol.* **2012**, *107*, 1613–1633. [[CrossRef](#)]
120. Canet, C.; Prol-Ledesma, R.M.; Proenza, J.A.; Rubio-Ramos, M.A.; Forrest, M.J.; Torres-Vera, M.A.; Rodriguez-Diaz, A.A. Mn-Ba-Hg mineralization at shallow submarine hydrothermal vents in Bahia Concepcion, Baja California Sur, Mexico. *Chem. Geol.* **2005**, *224*, 96–112. [[CrossRef](#)]
121. Seyfried, W., Jr.; Bischoff, J. Experimental seawater-basalt interaction at 300 °C, 500° bar: Chemical exchange, secondary mineral formation and implications for the transport of heavy metals. *Geochim. Cosmochim. Acta* **1981**, *45*, 135–147. [[CrossRef](#)]
122. Blount, C.W. Barite solubilities and thermodynamic quantities up to 300 degrees C and 1400 bars. *Am. Mineral.* **1977**, *62*, 942–957.
123. Berndt, M.E.; Seyfried, W.E., Jr.; Beck, J.W. Hydrothermal alteration processes at midocean ridges: Experimental and theoretical constraints from Ca and Sr exchange reactions and Sr isotopic ratios. *J. Geophys. Res. Solid Earth* **1988**, *93*, 4573–4583. [[CrossRef](#)]
124. Von Damm, K.L. Systematics of and postulated controls on submarine hydrothermal solution chemistry. *J. Geophys. Res. Solid Earth* **1988**, *93*, 4551–4561. [[CrossRef](#)]
125. Mills, R.; Teagle, D.; Tivey, M. Fluid mixing and anhydrite precipitation within the TAG mound. *Proc. Ocean Drill. Program Sci. Results* **1998**, *158*, 119–127.
126. Elderfield, H.; Mills, R.A.; Rudnicki, M.D. Geochemical and thermal fluxes, high-temperature venting and diffuse flow from mid-ocean ridge hydrothermal systems: The TAG hydrothermal field, Mid-Atlantic Ridge 26°N. *Geol. Soc. Lond. Spec. Publ.* **1993**, *76*, 295–307. [[CrossRef](#)]
127. Shanks, W.C.I. Stable Isotopes in Seafloor Hydrothermal Systems: Vent fluids, hydrothermal deposits, hydrothermal alteration, and microbial processes. In *Reviews in Mineralogy and Geochemistry*; Mineralogical Society of America: Chantilly, VA, USA, 2001; Volume 43, pp. 469–525.
128. Ono, S.; Wing, B.; Johnston, D.; Farquhar, J.; Rumble, D. Mass-dependent fractionation of quadruple stable sulfur isotope system as a new tracer of sulfur biogeochemical cycles. *Geochim. Cosmochim. Acta* **2006**, *70*, 2238–2252. [[CrossRef](#)]
129. Peters, M.; Strauss, H.; Petersen, S.; Kummer, N.-A.; Thomazo, C. Hydrothermalism in the Tyrrhenian Sea: Inorganic and microbial sulfur cycling as revealed by geochemical and multiple sulfur isotope data. *Chem. Geol.* **2011**, *280*, 217–231. [[CrossRef](#)]
130. Peters, M.; Strauss, H.; Farquhar, J.; Ockert, C.; Eickmann, B.; Jost, C.L. Sulfur cycling at the Mid-Atlantic Ridge: A multiple sulfur isotope approach. *Chem. Geol.* **2010**, *269*, 180–196. [[CrossRef](#)]
131. Rouxel, O.; Shanks, W.C., III; Bach, W.; Edwards, K. Integrated Fe- and S-isotope study of seafloor hydrothermal vents at East Pacific Rise 9–10°N. *Chem. Geol.* **2008**, *252*, 214–227. [[CrossRef](#)]

132. Rouxel, O.; Ono, S.; Alt, J.; Rumble, D.; Ludden, J. Sulfur isotope evidence for microbial sulfate reduction in altered oceanic basalts at ODP Site 801. *Earth Planet. Sci. Lett.* **2008**, *268*, 110–123. [[CrossRef](#)]
133. McKibben, M.A.; Eldridge, C. Radical sulfur isotope zonation in pyrite accompanying boiling and epithermal gold deposition; a SHRIMP study of the Valles Caldera, New Mexico. *Econ. Geol.* **1990**, *85*, 1917–1925. [[CrossRef](#)]
134. Ohmoto, H.; Goldhaber, M.B. Sulfur and Carbon Isotopes. In *Geochemistry of Hydrothermal Ore Deposits*, 3rd ed.; Barnes, H.L., Ed.; Wiley: New York, NY, USA, 1997; pp. 517–612.
135. Herzig, P.M.; Hannington, M.D.; Arribas, A., Jr. Sulfur isotopic composition of hydrothermal precipitates from the Lau back-arc: Implications for magmatic contributions to seafloor hydrothermal systems. *Miner. Depos.* **1998**, *33*, 226–237. [[CrossRef](#)]
136. Kusakabe, M.; Komoda, Y.; Takano, B.; Abiko, T. Sulfur isotopic effects in the disproportionation reaction of sulfur dioxide in hydrothermal fluids: Implications for the $\delta^{34}\text{S}$ variations of dissolved bisulfate and elemental sulfur from active crater lakes. *J. Volcanol. Geotherm. Res.* **2000**, *97*, 287–307. [[CrossRef](#)]
137. Giggenbach, W.F. Chemical Composition of Volcanic Gases. In *Monitoring and Mitigation of Volcano Hazards*; Springer: Berlin/Heidelberg, Germany, 1996; pp. 221–256.
138. Sillitoe, R.H.; Hedenquist, J.W. Linkages between volcanotectonic settings, ore-fluid compositions, and epithermal precious metal deposits. *Spec. Publ. Soc. Econ. Geol.* **2003**, *10*, 315–343.
139. Petersen, S.; Herzig, P.M.; Hannington, M.D.; Jonasson, I.R.; Arribas, A. Submarine gold mineralization near Lihir Island, New Ireland fore-arc, Papua New Guinea. *Econ. Geol.* **2002**, *97*, 1795–1813. [[CrossRef](#)]
140. Minniti, M.; Bonavia, F.F. Copper-ore grade hydrothermal mineralization discovered in a seamount in the Tyrrhenian Sea (Mediterranean): Is the mineralization related to porphyry-coppers or to base metal lodes? *Mar. Geol.* **1984**, *59*, 271–282. [[CrossRef](#)]
141. Naden, J.; Kiliyas, S.P.; Darbyshire, D.P.F. Active geothermal systems with entrained seawater as modern analogues for transitional volcanic-hosted massive sulfide and continental magmato-hydrothermal mineralization: The example of Milos Island, Greece. *Geology* **2005**, *33*, 541. [[CrossRef](#)]
142. Hedenquist, J.W.; Arribas, A.; Gonzalez-Urien, E. Exploration for Epithermal Gold Deposits. *SEG Rev.* **2000**, *13*, 245–277.
143. Hannington, M.D.; Scott, S.D. Sulfidation equilibria as guides to gold mineralization in volcanogenic massive sulfides; evidence from sulfide mineralogy and the composition of sphalerite. *Econ. Geol.* **1989**, *84*, 1978–1995. [[CrossRef](#)]
144. Sillitoe, R.H.; Hannington, M.D.; Thompson, J.F.H. High sulfidation deposits in the volcanogenic massive sulfide environment. *Econ. Geol.* **1996**, *91*, 204–212. [[CrossRef](#)]
145. Yeats, C.J.; Parr, J.M.; Binns, R.A.; Gemmell, J.B.; Scott, S.D. The SuSu Knolls Hydrothermal Field, Eastern Manus Basin, Papua New Guinea: An Active Submarine High-Sulfidation Copper-Gold System. *Econ. Geol.* **2014**, *109*, 2207–2226. [[CrossRef](#)]
146. Anderson, M.O.; Hannington, M.D.; McConachy, T.F.; Jamieson, J.W.; Anders, M.; Wienkenjoham, H.; Strauss, H.; Hansteen, T.; Petersen, S. Mineralization and alteration of a modern seafloor massive sulfide deposit hosted in mafic volcanoclastic rocks. *Econ. Geol.* **2019**, 857–896. [[CrossRef](#)]
147. Hannington, M.D.; Jamieson, J.W.; Monecke, T.; Petersen, S. Modern sea-floor massive sulfides and base metal resources: Toward an estimate of global sea-floor massive sulfide potential. In *The Challenge of Finding New Mineral Resources: Global Metallogeny, Innovative Exploration, and New Discoveries*; Goldfarb, R., March, E.E., Monecke, T., Eds.; Society of Economic Geologists: Littleton, CO, USA, 2010; Volume 2, pp. 317–338.

